Energy & Environmental Science

ROYAL SOCIETY OF CHEMISTRY

PERSPECTIVE

View Article Online
View Journal | View Issue

Cite this: *Energy Environ. Sci.*, 2024, **17**, 1368

Enhancing the inherent stability of perovskite solar cells through chalcogenide-halide combinations

Cheng Wang,[a] Riming Nie,*[ab] Yiming Dai,[a] Huanyu Tai,[a] Bingjian Zhu,[a] Luyao Zhao,[a] Yong Wu,[a] Wanlin Guo*[a] and Sang Il Seok*[b]

Perovskite solar cells have attracted much attention due to their rapidly increasing power conversion efficiency, however, their poor inherent long-term stability limits their commercialization. One of the reasons for the low stabilities of halide perovskites can be attributed to the weak ionic binding energy between the monovalent halide and divalent lead ions. Here, we present an overview of several strategies for combining chalcogenides and halides to enhance the inherent stability of perovskite materials. Firstly, incorporating chalcogenides into halide perovskite materials can improve their ionic binding energies. However, it is important to note that this method can only improve their stability somewhat. Secondly, the exploitation of chalcogenide perovskite materials has the potential to significantly improve the inherent stability of perovskite materials. Nevertheless, their efficiencies remain relatively low, and the device fabrication needs high-temperature annealing and expensive experiments. Thirdly, the concept of combining chalcogenides and halides to create new perovskite materials shows promise, however, there is still limited research in this direction. Finally, we offer a perspective on the future development direction and trends of these three research areas.

Received 24th October 2023,
Accepted 12th January 2024

DOI: 10.1039/d3ee03612j

rsc.li/ees

Broader context

As the world increasingly looks towards sustainable energy sources, perovskite solar cells have emerged as a promising alternative to traditional silicon-based photovoltaics, primarily due to their remarkable rise in power conversion efficiency. Nevertheless, their journey towards widespread commercialization faces a critical hurdle - the long-term stability of these materials. The precarious nature of halide perovskites, exemplified by their susceptibility to environmental factors, is a significant roadblock. It stems from the weak ionic binding energy between the monovalent halide and divalent lead ions within their crystal lattice. Within this context, this perspective provides an insightful exploration of strategies aimed at fortifying the stability of perovskite materials. The multi-dimensional landscape of potential solutions includes the introduction of chalcogenides into halide perovskites, a method that demonstrates notable improvements in ionic binding energies, although it does not entirely resolve the stability issues. On the other hand, delving into the unique properties of chalcogenide perovskite materials holds promise for significantly bolstering stability. Yet, the inherent trade-offs between stability and efficiency, along with the resource-intensive fabrication processes, must be carefully weighed. Additionally, the innovative approach of blending chalcogenides and halides to forge novel perovskite materials is a burgeoning frontier. However, it still remains relatively uncharted, necessitating further exploration. Consequently, the potential for a more stable, efficient, and cost-effective photovoltaic future is a tantalizing prospect that resonates with the broader goals of environmental sustainability and reduced dependence on fossil fuels. This broader context underscores the significance of ongoing research and the potential impact of the directions outlined in this overview.

1. Introduction

In 2009, Miyasaka *et al.* introduced perovskite-sensitized solar cells as a noble alternative to traditional dye-sensitized solar cells (DSSCs), offering the potential for more efficient light absorption.[1] Initially, these cells demonstrated a low efficiency of only 3.81%. The chemical composition of halide perovskite materials is represented by the formula ABX_3. In this structure, the A site accommodates a positive monovalent metal cation, the B site hosts a divalent cation, and the BX_6 arrangement

[a] *State Key Laboratory of Mechanics and Control of Mechanical Structures, Key Laboratory for Intelligent Nano Materials and Devices of the Ministry of Education, Institute for Frontier Science, College of Mechanical and Electrical Engineering, Nanjing University of Aeronautics and Astronautics, Nanjing 210016, P. R. China. E-mail: rmnie@nuaa.edu.cn, wlguo@nuaa.edu.cn*

[b] *Department of Energy Engineering, School of Energy and Chemical Engineering, Ulsan National Institute of Science and Technology, 50 UNIST-gil, Eonyang-eup, Ulju-gun, Ulsan 44919, Republic of Korea. E-mail: seoksi@unist.ac.kr*

exhibits classical octahedral connectivity.[2] Typically, monovalent cations at the A site include MA^+, FA^+, or Cs^+, while divalent cations at the B site are represented by Pb^{2-}, Sn^{2-}, or Ge^{2-}, and halides at the X site are Cl^-, Br^-, or I^-. The perovskite crystal structure comprised an A^+ ion at the center of the BX_6 octahedron, with the B^{2-} ion exhibiting six-way coordination. Surrounding these ions are octahedra formed by halide anions, creating a unique perovskite crystal structure.[3] Furthermore, these structures allow for the accommodation of various other elements, significantly expanding the range of perovskite composition. However, a challenge arises as most perovskite materials are susceptible to dissolving in the liquid electrolyte used in DSSCs, leading to rapid degradation in the device performance. To address this issue, researchers replaced the liquid electrolyte of DSSCs with a solid-state hole-transporting material (HTM), resulting in the fabrication of solid-state perovskite-sensitized solar cells.[3] In 2014, Seok *et al.*[4] proposed an anti-solvent method to deposit high-quality perovskite films, leading to significant advancements in real perovskite solar cells (PSCs). Subsequently, the anti-solvent method became a prominent technique for fabricating high-efficiency and stable PSCs. Notably, planar PSCs have recently made substantial progress, achieving a certified efficiency of 26.1%.[5]

The advancement in PSCs increased their efficiency to around 26%[5,24–33] through structural optimization. These improvements involve mesoporous titanium dioxide, the design of organic and inorganic carrier transport layers, adjustment of doping and composition with various additives, and enhancement in device structures, including the development of laminated solar cells. All these efforts aim to design and synthesize high-efficiency PSCs with long-term stability. However, there remains a considerable gap in stability compared to monocrystalline silicon inorganic solar cells. Therefore, how to efficiently design and synthesize long-term stable perovskite materials is the main research direction of researchers.

First, this review summarizes the work on improving stability for halide PSCs with high power conversion efficiency. Secondly, we discuss chalcogenide-based solar cells' long-term stability and high hydrophobicity. Thirdly, it is envisaged that an effective strategy to improve the stability of perovskite materials is to mix chalcogenide and halide perovskites. Finally, we propose the future research direction for mixed chalcogenide and halide PSCs.

2. Halide perovskite solar cells

Undoubtedly, in recent years, with the continuous improvement of the efficiency of halide PSCs, their poor chemical and environmental stability has also been exposed. After exposure for a long time, the crystal structure of halide perovskites will undergo phase change and decomposition, resulting in degraded performance. In addition, these solar cells are very sensitive to humid environments and oxygen, which further limits their stability in practical applications. This is a major factor limiting the commercialization of perovskites. Therefore, there is an urgent need to find stable alternatives in the natural environment, and researchers have adopted various strategies. Among them, the introduction of more stable sulfur elements has attracted much attention. Considering the atomic structure of chalcogenides and the stability of lone pair electrons, the interaction of metals with sulfur atoms in chalcogenides is more covalent, which makes the overall covalent bond of the material stronger, thereby improving stability.[44] The introduction of chalcogenides into PSCs can significantly improve the device efficiency and stability.

2.1. Chalcogenides in hole transport layers

One of the primary areas of research involves the incorporation of sulfur into the hole transport layer of PSCs. Considering the dipole moment interaction of the lone pair electrons of chalcogenides (such as sulfur S and oxygen O) with the unpaired Pb^{2+} of perovskites, the long-term stability of PSCs can be significantly improved. A typical application is methoxy interactions in trainline structures such as spiro-OMeTAD, which has been widely used as various doped/undoped hole transport layers, where derivatives substituted by ortho-methoxy groups exhibit higher LUMO (Lowest Unoccupied Molecular Orbital) levels and can effectively block electrons. At the same time, it has good solubility, weak absorption in the visible light range, good film-forming ability, and high hole mobility. However, it has the disadvantages of high processing cost, difficult purification, and low conductivity. It is necessary to improve its electrical performance by doping ion salts, which will cause problems with device stability.[45] Pentaerythritol tetra (3-mercaptopropionate) (PETMP), an aliphatic crosslinker containing four mercaptan groups, has been employed to form anti-Markovnikov sulfide through mercaptan-alkene reaction. This process results in the production of cross-linked HTLs, significantly enhancing their photothermal stability even without additional packaging.[46–48] Additionally, various approaches exist to bolster perovskite stability by establishing molecular interactions with chalcogenide elements. These strategies find extensive application in diverse types of hole transport materials.[49] In 2021, Wong *et al.* deposited bifunctional aluminum-doped CuS films in p–i–n structure PSCs as the HTL, which not only played the role of an HTL but also improved the crystallization of perovskites at the interface. Characterization of Urbach energy, light intensity, and open circuit voltage showed that a better-quality interface was formed in the sulfide HTL–perovskite heterojunction. The degradation behaviour of sulphide-HTL-based perovskite devices was studied. It has been observed that the equipment remains at close to 95% of its initial efficiency after 2 weeks in a controlled environment[50] (Fig. 1c).

2.2. Chalcogenides in perovskite layers

Of course, there are many improvements and modifications to the use of chalcogenide compounds in the preparation of PSCs. These sulfide elements can effectively promote the crystallization performance and stability of halide PSCs. The most widespread impact was the introduction of sulfur (S_8) into the

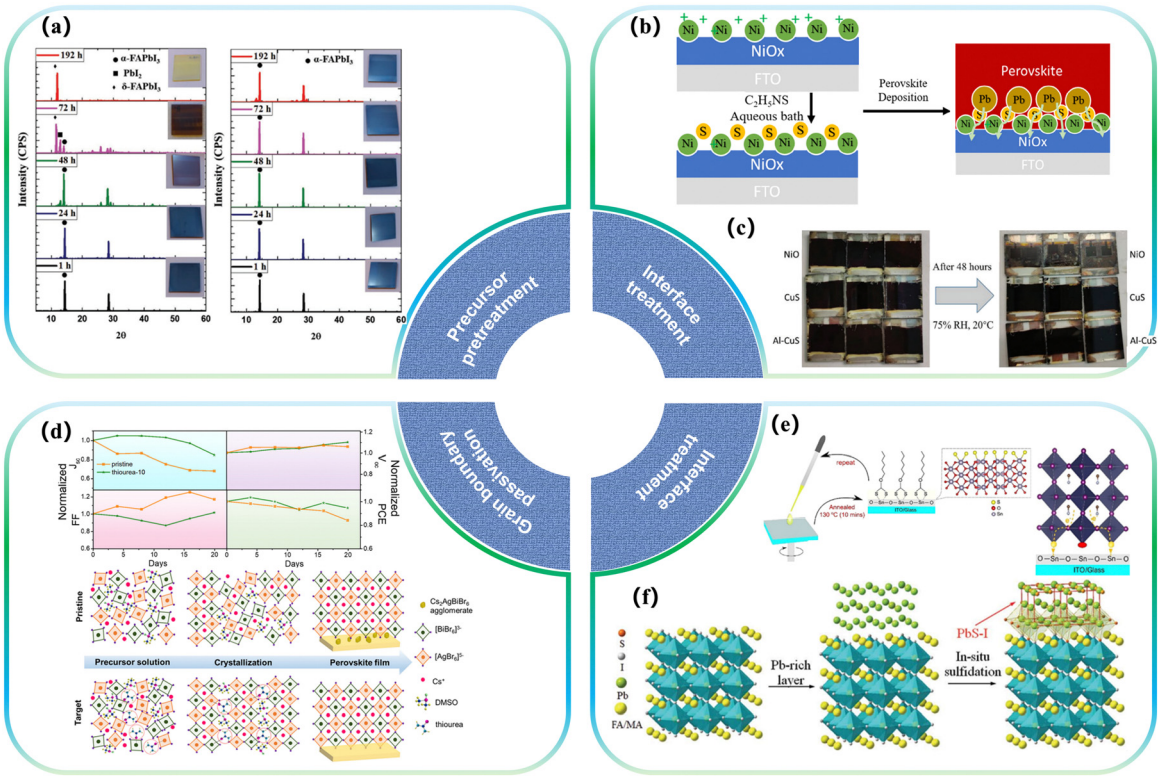

Fig. 1 Effect of partial sulfides on the modification of perovskites. (a) XRD patterns of films deposited from a precursor solution aged for times ranging from 1 to 192 h without (left) and with (right) sulfur additives.[51] Copyright 2019, Advanced Energy Materials. (b) Schematic illustration of the S doping process on the NiO surface.[52] Copyright 2020, Solar RRL. (c) The visible degradation of the devices after storing them in 75% RH and 20 °C humidity for 48 h; the left-hand side shows the initial images of the devices, and the right-hand side shows the device images after 48 h. The top row of the devices is NiO, the middle row is CuS, and the bottom row is Al-CuS.[50] Copyright 2020, Advanced Functional Materials. (d) Normalized performance parameters for the pristine $Cs_2AgBiBr_6$, thiourea-10 cells in the stability test under ambient conditions without any encapsulation, and the proposed mechanism of $Cs_2AgBiBr_6$ film formation assisted by a thiourea additive.[53] Copyright 2022, Journal of Colloid and Interface Science. (e) Sulfur-functionalized electron transport layer formed by xanthate annealing and device interfacial structure.[54] Copyright 2018, ChemSusChem. (f) Schematic diagram of SST vulcanization.[55] Copyright 2022, Science.

halide perovskite precursor discovered by Seok *et al.* in 2019, which greatly stabilized the precursor solution due to amine-sulfur coordination without affecting the PCE of the derived PSC. At the same time, the introduction of sulfur to stabilize the precursor solution can improve the stability of PSCs (Fig. 1a).[51] In 2020, Chen *et al.* prepared perovskite films to reduce defects by using a lead indicator (dithizone) as an additive to the perovskite layer. Dithizone can slow down the crystallization rate of perovskite films, passivate defects, and enhance the structural stability of perovskite films by coordinating with lead atoms. As a result, dithizone-doped devices have excellent PCE and stability.[56] In 2022, Zhou *et al.* studied the effects of sulfur cations on the evolution of two-dimensional Ruddlesden–Popper (2DRP) perovskite intermediates and photovoltaic performance. The introduction of sulfur cations leads to preferential intermediate conversion of perovskites and improvement of film quality. Due to reduced recombination and enhanced charge transfer, the resulting device provides a championship efficiency of 19.08% at room temperature and an optimal efficiency of 20.52% at 180 K. What's more, the unpackaged device maintains an 84% initial efficiency over 1000 h with a maximum power point (MPP) track of 40 °C.[57]

Shao *et al.* delayed the crystallization of the $Cs_2AgBiBr_6$ perovskite by introducing Lewis's base additive into the precursor solution. The addition of the strongly coordinated thiourea additive and sulfur donor led to the formation of Lewis acid–base adducts, delayed the crystallization process of $Cs_2AgBiBr_6$ crystals, improved the quality of $Cs_2AgBiBr_6$ films, reduced defect density, inhibited charge carrier recombination, and showed excellent stability. After 20 days of storage in air, the PCE retention was 95% (Fig. 1d).[53] In 2023, Finkenauer *et al.* modified the crystal growth process of halide PSCs by introducing phenylmercaptan/selenol. In the second step, the combination of phenylselenol and amine ligands in the precursor solution dramatically changes the chemistry of the solution, increasing the conversion rate of PbI_2 to films with high crystallization and orientation of α-$FAPbI_3$.[58] In conclusion, this method plays an important role in improving the stability and efficiency of the device.

2.3. Chalcogenides in interface layers

In 2018, Hayase *et al.* reported a strategy to effectively passivate charge traps and reduce interfacial recombination by functionalizing the surface of SnO_2 with sulfur. The results show that

the sulfur-functionalized atoms can coordinate with the undercoordinated Pb^{2+} near the interface, and the interfacial sulfur functionalization accelerates the interfacial charge transfer kinetics and reduces the traps in the perovskite block. The non-sealed interface of sulfur-functionalized solar cells also showed a considerable delay in solar cell degradation, degrading only 10% after 70 days of air storage[54] (Fig. 1e). In 2020, Yang *et al.* introduced a sulfur doping strategy, which modifies the NiO surface through ion exchange reaction through simple and scalable chemical bath deposition technology, thereby greatly improving the photovoltaic performance of derived devices. Systematic studies were performed in which it was demonstrated that sulfur doping can generate favorable interfacial energy and reduce V_{OC} loss. Pb–S interaction also improves the quality of perovskite films, reduces the number of grain boundaries, reduces the formation of structural defects, and improves the conductivity and stability of directly adjacent perovskite layers[52] (Fig. 1b).

Next, Jiang *et al.* introduced lead sulfide (PbS) into the perovskite film surface by performing an *in situ* reaction with thioacetamide (TAA) in solution. The PbS layer significantly reduces the trap density of the perovskite film and improves the charge extraction efficiency of the perovskite to the external charge transfer layer. In addition, it was also found that the water-insoluble PbS layer can effectively protect the perovskite film from water penetration. As a result, PSCs showed a stable output efficiency of 22.04% and high stability.[59] In 2022, Fang *et al.* constructed a stable perovskite heterojunction for inverted solar cells by sulfidation of Pb-rich perovskite thin films. The lead–sulfur (Pb–S) bond formed increases the Fermi level at the perovskite interface and creates an additional backfield for electron extraction. Strong Pb–S bonds can stabilize the perovskite heterostructure and enhance the potential perovskite structure with a similar lattice. Surface vulcanization devices retain more than 90% of the initial PCE after 2200 h of aging at 85 °C or 1000 h of operation at the maximum power point under continuous illumination at 55 ± 5 °C (Fig. 1f).[55] In addition, Wang *et al.* used 2-mercaptopyridine (2-MP) to surface-treat halide PSCs, because 2-MP contains nitrogen and sulfur heteroatoms, which have lone pair electrons and can act as Lewis bases. The optimized device shows impressive operational stability. After a maximum power point tracking experiment for 1000 h at 40 °C, the efficiency was reduced by 16%. However, since 2-MP cannot enter the perovskite lattice, only passivation and external treatment can be performed.[60] At the same time, the environmental storage stability of the unencapsulated device is significantly improved, maintaining an initial efficiency of more than 80% after 600 h.

2.4. Chalcogenide quantum dots

As early as 2018, Han *et al.* added PbS quantum dots into $CH_3NH_3PbI_3$ ($MAPbI_3$) precursors to form a QD-in-perovskite structure, which is beneficial to the crystallization of perovskites, resulting in an increase in particle size, a decrease in fragmentation particles, an enhancement of characteristic peak intensity, a large proportion of (220) planes in X-ray diffraction patterns, and a highly regular and large crystal structure.[61] Gaulding *et al.* carefully investigated the effects of surface chemistry and antisolvent on the emission and morphological properties of perovskite films embedded in metal halide PSCs. Compared with pure $MAPbI_3$ thin films, the apparent grain size of $MAPbI_3$ with a PbS quantum dot structure is smaller, and of course, it will also be taken into account that the choice of antisolvent will affect the growth mode of $PbS/MAPbI_3$ perovskite crystals.[62] Lee *et al.* synthesized quantum dots (QDs) composed of copper (Cu), zinc (Zn), indium (In), sulfur (S), and selenium (Se) in 2020 and doped them into $CsPbBr_3$ inorganic perovskite films. To disperse $CsPbBr_3$-encapsulated CZISSe-QDs in $PbBr_2$ solution, the inorganic $CsPbBr_3$ shell was replaced by ligand exchange. CZISSe-QDs act as the seeds of crystal nucleus in $PbBr_2$ films, promoting the crystallization of $CsPbBr_3$. In addition, they are present in the mesoporous TiO_2-$CsPbBr_3$ perovskite layer, which facilitates electron extraction and transport from the $CsPbBr_3$ photoabsorbing layer to TiO_2.[63] These works on quantum dots achieve a finer and more regular lattice structure through the interaction of sulfur elements, which can significantly improve its stability to the environment and extend the lifetime of the device.

2.5. Other ways to introduce chalcogenides

In the process of introducing sulfur into PSCs, it can be incorporated not only within PSCs but also through other ways. Introducing anions of organic structures, such as thiocyanate ions, is a common method for improving their crystallization ability and surface morphology in PSCs.[64–70] As early as 2015, Jiang *et al.* replaced the two iodines in $CH_3NH_3PbI_3$ with amphoteric halides of thiocyanate (SCN^-), and fabricated PSCs related to $CH_3NH_3Pb(SCN)_2I$ by a simple spin-coating process, which generally maintained a lattice structure similar to halogen perovskites due to thiocyanate ions.[71] In addition, in 2016, Tai *et al.* used a simple precursor solution treatment method to show that PSCs are prepared under environmental conditions using the lead(II) thiocyanate ($Pb(SCN)_2$) precursor, and high-quality $CH_3NH_3PbI_{3-X}(SCN)_X$ perovskite films can be easily prepared even if the relative humidity exceeds 70%.[72] In the same year, Liu *et al.* also introduced thiocyanate into PSCs containing lead thiocyanate at room temperature. Due to the properties of thiocyanate, PSCs with $(MA)_2Pb(SCN)_2I_2$ structures can be fabricated at a low temperature of 70 °C.[73]

All in all, PSCs have gradually reached people's expectations in terms of performance, with a PCE of up to 26%, making them a leading technology in solar cells. However, their stability and sensitivity to water and oxygen present significant challenges that need to be solved. The former severely limits the environmental conditions for the use of these devices. The latter places further specific requirements on the processing conditions. Therefore, it is imperative to focus on designing and enhancing the stability of the active layer in PSCs.

3. Chalcogenide inorganic thin film solar cells

Compared with high-efficiency halide PSCs, chalcogenide inorganic thin film solar cells have attracted much attention due to their excellent long-term water and oxygen stability.[74–76] As mentioned earlier, the perovskite-type crystal structure under the ABX_3 structure is usually cubic and orthorhombic. In this traditional case, we generally use the X structure as a halide anion, of course, it is also modified by the chalcogenide anion. For halide PSCs, the stability of PSCs can be significantly improved by introducing sulfur into anions, enabling lighter adaptability to the environment and demand.[77,78] To form perovskites with chalcogenide structures (*i.e.*, X = O^{2-}, S^{2-}, and Se^{2-}), based on these two points, the direct selection of the A site falls on the alkaline earth elements, and many other metal elements have a bivalent structure for reference.

3.1. Theoretical calculations

Under these limitations, there are theoretically 3744 possible element groups forming the chalcogenide perovskite.[79] However, only a limited number of these compositions are thermodynamically stable and will crystallize in the desired cubic or pseudo-cubic perovskite structure. Based on purely geometric considerations, the ion radius of the atoms in the composition can be used to calculate the Goldschmidt tolerance factor (t) and octahedral factor (μ) to predict the stability and formability of a specific perovskite form.[80,81] It is expressed as:

$$t = \frac{r_A + r_X}{\sqrt{2}(r_B + r_X)} \quad (1)$$

$$\mu = \frac{r_B}{r_X} \quad (2)$$

where r_A, r_B and r_X are the ionic radii of the A-site cation, B-site cation, and X-site anion, respectively. Based on the values of t and μ, the most stable form can be predicted.

In a strict sense, the main structures of perovskites include the $GdFeO_3$ type and $TaAgS_3$ type. In the latter type, B cations move slightly from the center of their BX_6 octahedron. While other structures do not possess the properties of traditional perovskite crystal structures, they are still categorized as perovskite structures due to their elemental composition and inherent properties. Fig. 2 outlines the perovskite structure of the chalcogenide ABX_3. The primary relevant structure is the $GdFeO_3$ structure, often referred to as the β-phase structure, which typically forms at higher temperatures during processing.

Compared to traditional halide PSCs, chalcogenides are challenging to synthesize, particularly due to the bonding requirements for the selenium-based structures. Thus, the current research on pure chalcogenide thin-film solar cells is more important. The developments and improvements lie in the field of theoretical simulation computing, and the computational methods envisaged by the researchers can better guide the development of synthesis work. After the introduction of

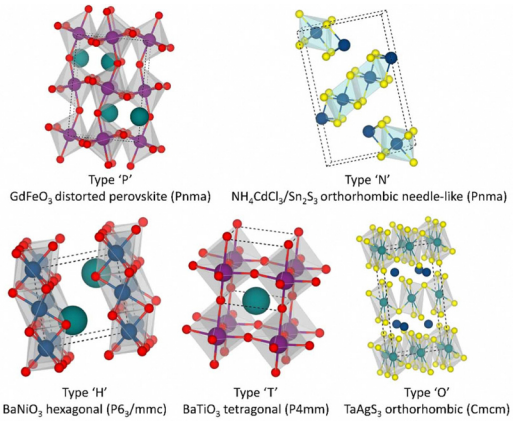

Fig. 2 Perovskite structure of the chalcogenide ABX_3. The cell diagram of the crystal structure of chalcogenide perovskites, as well as their geometric shape, space group, and prototype composition.[82] Copyright 2021 Devendra Tiwari *et al.* J. Phys. Energy.

metal sulfides, there will be 168 chalcogenide ABX_3 compounds (A = Mg, Ca, Sr, Ba, Zn, Cd, Sn, Pb; B = Ti, Zr, Hf, Si, Ge, Sn, Pb; X = O, S, Se) with four different crystal structures (group symmetry *Pm3m*, Pnma, P63/mmc and Pnma (needle)). The band gap, light absorption, current-carrying effective mass, phase stability, thermodynamic stability, and dynamic stability were analysed, and these materials were screened out for photovoltaic applications. The potential of orthorhombic perovskites $BaZrS_3$, $BaHfSe_3$, $SrZrSe_3$, $SrHfSe_3$, and $BaZrSe_3$ has been demonstrated for solar cell applications[83,84] (Fig. 3b).

$SrSnSe_3$ and $SrSnS_3$ are expected to be direct bandgap semiconductors with bandgap values in the optimal range of 0.9–1.6 eV. $SrSnSe_3$ and $SrSnS_3$ perovskites not only have good light absorption properties and carrier mobility, but also have flexible band gaps that can be continuously adjusted in the range of 0.9–1.6 eV by element mixing strategies, and these desirable properties give $SrSnSe_3$ the potential to be a high-efficiency solar absorbing material, opening up possibilities for the design of chalcogenide solar cells[86] (Fig. 3c). In 2019, Nag and his colleagues reviewed a series of chalcogenide perovskites with an appropriate band gap, strong absorption coefficient, and low effective carrier mass obtained by calculation. The theoretical maximum PCE of these materials is close to 30%. Under the guidance of these theoretical predictions, compounds such as $BaZrS_3$, $SrZrS_3$, and layered perovskite $Ba_3Zr_2S_7$ were successfully synthesized. The experimentally obtained direct bandgap of $BaZrS_3$ (~1.8 eV) and $SrZrS_3$ (~2.1 eV) is slightly higher, but the direct bandgap of $Ba_3Zr_2S_7$ (~1.3 eV) is close to the ideal bandgap for single-junction solar cell applications. These materials exhibit strong absorption coefficients and near-band-edge emission characteristics. Zr-chalcogenides are promising solar harvesters, but achieving their efficacy in solar cell performance requires fabricating high-quality thin films and optimizing the charge transport process.[85] At present, the synthesis and processing of chalcogenide perovskites pose greater challenges compared to halide

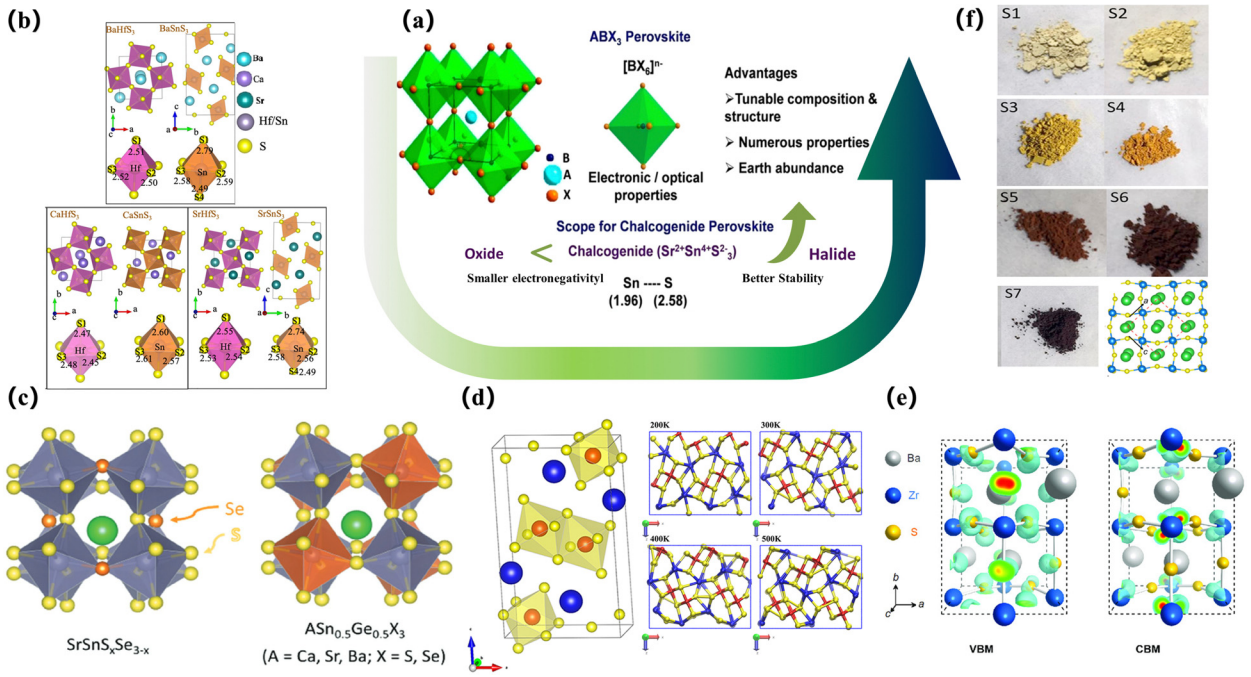

Fig. 3 The simulated lattice structure of the sulfide perovskite. (a) Intuitive benefits of chalcogenide perovskites.[85] Copyright 2019, Chem. Mater. (b) Crystal structures. $BaHfS_3$ in orthorhombic distorted phase and$BaSnS_3$ in needle-like phase; $CaHfS_3$ and$CaSnS_3$ in orthorhombic distorted phase; $SrHfS_3$ in orthorhombic distorted phase and $SrSnS_3$ in needle-like phase. Sulfur atom projected density of states.[83] Copyright 2022, J. Phys. Chem. Lett. (c) Crystal structures of ABX_3 perovskite chalcogenides with either a perfect perovskite structure or a distorted perovskite structure.[86] Copyright 2017, Advanced Energy Materials (d) Snapshots of the $BaZrSe_3$ crystal at different temperatures ranging from 200 K to 500 K. The projection of the structure is along the *y*-axis. Blue spheres represent Ba atoms, red spheres represent Zr atoms, and yellow spheres represent Se atoms.[87] Copyright 2019, Journal of Applied Physics. (e) Charge density profiles of $BaZrS_3$ for the bands of the VBM and CBM;[7] Copyright 2020, Solar RRL. (f) The optical images of the BaZr-oxysulfides with different degrees of sulfurization and the top view of $BaZrS_3$ in the distorted perovskite structure (space group Pnma). Red dashed frames and black arrows mark the unit cell and the crystallographic orientations, respectively.[88] Copyright 2016, Nano Energy.

perovskites. Both computational and experimental material design challenges need to be addressed in the near future. In particular, numerous chalcogenide perovskites have the advantages of earth-abundant resources, environment friendly nature, and robust thermal and humidity stability. Concurrently, Ong *et al.* studied the kinetic stability of $BaZrSe_3$ formed by replacing S in $BaZrS_3$ with selenium at non-zero temperature. They thermalized the predicted zero-temperature crystal structure of $BaZrSe_3$ at different temperatures from 200 to 500 K by phonon frequency calculations and *ab initio* molecular dynamics simulations. The results show that the dynamic changes of the system have no obvious changes on the shells of BaSe and ZnSe at different temperatures, and the same structural units remain unchanged. Therefore, $BaZrSe_3$ is predicted to be stable under typical conditions[87] (Fig. 3d).

Machine learning methods have also been used to screen dichalcogenide perovskites for photovoltaic applications. Agiorgousis *et al.* developed a method based on a machine learning algorithm that uses atomic data from the periodic table to select potential absorber materials.[89] By considering the thermodynamic stability, kinetic stability, and light absorption properties of the materials, they found that Ba_2AlNbS_6, Ba_2GaNbS_6, Ca_2GaNbS_6, Sa_2GaNbS_6, Sr_2InNbS_6, and Ba_2SnHfS_6 are the most promising new photovoltaic absorbers to replace $CH_3NH_3PbI_3$.

3.2. Experimental research

3.2.1. High-temperature solid-phase synthesis method. Currently, one of the biggest challenges for chalcogenide perovskites is their synthesis. Although the crystal structure and optoelectronic properties of the overall sulfur-containing structure are similar to those of traditional halide PSCs, the synthesis method is completely different. This may be due to the valence state and crystal structure of the chalcogenides. So far, there are few perovskite-type materials of sulfides, but the structure of selenides has not been fully obtained. Of course, part of the work is a selenium-sulfur anion blending structure. The common chalcogenide perovskite structure is $BaZrS_3$, which can be crystallized by the $GdFeO_3$ structure regardless of the processing and synthesis methods and temperature conditions. This is also an important factor in its extensive development in the field of pyrite-bearing PSCs.[6–8,88,90] In contrast, $SrZrS_3$ exhibits two distinct crystal phases depending on different synthesis methods and temperatures[6,7,9] (Fig. 4e).

It can be seen that most of the chalcogenide solar cells prepared in these experiments are synthesized by solid-state reaction.[10] A common processing method is to seal the element

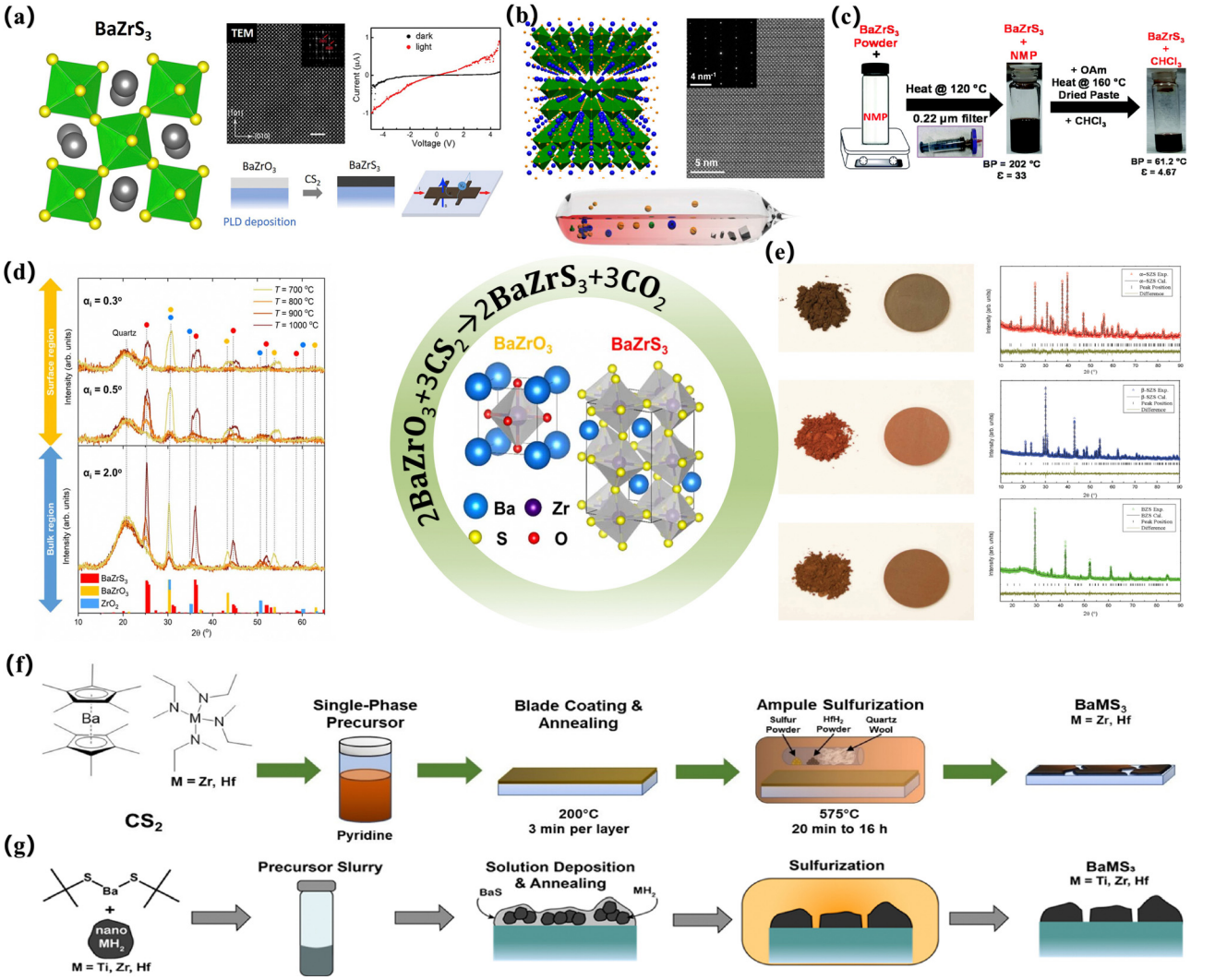

Fig. 4 Preparation of partially vulcanized thin film devices. (a) Atomically resolved HAADF image of a $BaZrS_3$ thin film sulfurized at 900 °C. The top right inset is the Fast Fourier Transformation (FFT) of the image. The *I*–*V* curves of the photodetector devices measured in the dark (black curves) and under illumination (red curves) for the $BaZrS_3$ films sulfurized at 1050 °C for 2 h;[91] Copyright 2020, Nano Energy. (b) A perspective view of the natural superlattice nanostructure in $Ba_3Zr_2S_7$. The blue, yellow, and green spheres represent Ba, S, and Zr atoms, respectively. The ZrS_6 octahedra are highlighted in green, the STEM image of a $Ba_3Zr_2S_7$ crystal is viewed along the a-axis, and the inset shows the corresponding SAED pattern.[16] Copyright 2018, Chem Mater. Phase identification of Ba–Zr–S–O thin films sulfurized at various temperatures: (c) schematic to make $BaZrS_3$ NCs colloidally stable in *N*-methyl-2-pyrrolidinone (NMP) followed by treatment with oleylamine (OAm) to make a dispersion in chloroform ($CHCl_3$).[92] Copyright 2021, Nanoscale. (d) Representative GIWAXS patterns of Ba–Zr–S–O films synthesized at different temperatures. The measurements were performed with grazing incidence angles (α_i) of 0.3°, 0.5° and 2°, allowing microstructural assessment of the surface ($\alpha_i \leqslant 0.5°$) and bulk ($\alpha_i = 2.0°$) regions of the thin films. Reference patterns of these phases are reported on the x-axis of the GIWAXS scans.[93] Copyright 2023, Santhanu Panikar Ramanandan *et al.* J. Phys. Energy. (e) Optical images of synthesized powders and pelletized samples and plots of powder XRD patterns with Rietveld analysis for α-$SrZrS_3$ (red), β-$SrZrS_3$ (blue), and $BaZrS_3$ (green).[6] Copyright 2016, Advanced Materials. (f) The synthesis procedure for the formation of $BaZrS_3$ and $BaHfS_3$. Cp*2Ba, $M(NMeEt)_4$ (M = Zr and Hf), and CS_2 were combined and allowed to react. Excess CS_2 was removed in-vacuo, and the resulting material was redissolved in pyridine to create a single-phase precursor ink. The ink was blade coated onto EXG glass and sulfurized at 575 °C in the presence of HfH_2 to create the ternary chalcogenide perovskites.[23] Copyright 2023, Angewandte Chemie International Edition. (g) Schematic outlining the synthesis method beginning with the use of Ba $(SCMe_3)_2$ and MH_2 (M = Ti, Zr, and Hf) nanopowders to make a slurry that is deposited on glass and annealed to make a mixture of BaS and MH_2. This material is then sulfurized to produce ternary $BaMS_3$ materials.[94] Copyright 2022, J. Am. Chem. Soc.

or binary chalcogenide precursors in ampoules and heat them at high temperatures for hours or days. This classical processing and growth method often requires a temperature of more than 1000 °C and a reaction cycle of several hours or even days, so that the reaction material can be completely diffused on a micron basis, to obtain a uniform crystalline material (Table 1). For example, Meng *et al.* converted the material into a quartz tube, sealed the quartz tube in a dynamic vacuum, and maintained the reaction mixture at 800 °C for nearly 15 h to achieve a good crystal structure.[11] As mentioned earlier, two twisted perovskite ($BaZrS_3$,[7] $SrZrS_3$,[7] $BaHfS_3$,[12] $SrHfS_3$,[12] $BaZr(S_{1-x}Se_x)_3$[7]) and non-perovskite materials ($PbHfS_3$,[95]

Table 1 Summarized reports on the synthesis and properties of chalcohalide materials

Material	Synthesis	Reaction conditions	Band gap(eV)	Ref.
$BaZrS_3$	Catalytic solid-state reaction	BaS+ Zr +I_2 + S,600 °C/60 h	1.81	6
α-$SrZrS_3$		SrS+ Zr +I_2 + S,850 °C/60 h	1.53	6
β-$SrZrS_3$		SrS+ Zr +I_2 + S,1000 °C/60 h	2.13	6
$BaZrS_3$	Solid-state reaction	BaS + $ZrSe_2$,1000 °C/48 h	1.94	7
$SrZrS_3$		SrS + ZrS_2,1000 °C/48 h	2.14	7
$SrHfS_3$		SrS + HfS_2,1100 °C/48 h	2.41	7
$BaHfS_3$		BaS + HfS_2,1200 °C/48 h	2.17	7
β-$LaYbS_3$	Solid-state reaction	M + Yb + Se + KI,1000 °C/96 h		8
$LaYbSe_3$				8
$CeYbSe_3$				8
$PrYbSe_3$				8
$NdYbSe_3$				8
$SmYbSe_3$				8
$BaZrS_3$	Two-step Solid phase vulcanization	$BaZrO_3$ + CS_2,1050 °C/6 h	1.75	9
$BaZrS_3$	Solid-state reaction	BaS +ZrS_2,900 °C/5 d		10
$BaZr_{1-x}Ti_xS_3$	Solid-state reaction	BaS +ZrS_2 + TiS_2,800 °C/15 h	1.47–1.7	11
$SrHfS_3$	Solid-state reaction	SrS +La_2S_3+ HfS_2,1100 °C/48 h	2.3	12
$EuZrS_3$	Solid-state reaction	Eu_2O_3 + ZrO_2 + KI + S,1000 °C/10 d	1.09	13
$BaZr_{-x}Ti_xS_3$	Two-step Solid phase vulcanization	$BaCO_3$, ZrO_2 + TiO_2,1000 °C/8 h; + CS_2, + 1050 °C/4 h	1.51–1.78	14
$BaZrS_3$	Sputtering	BaS +ZrS_2,3 h	1.8	15
$Ba_3Zr_2S_7$	Salt flux method	BaS+ Zr +S + $BaCl_2$,1050 °C/40 h	1.28	16
$Ba_4Zr_3S_{10}$				17
$Sr_{1+x}TiS_3$	Chemical vapor transport	SrS+ TiS_2 +I_2 + S,1000 °C/60 h		18
$NaTaO_3$	Ultrasonic method	NaAcO + AcOH rt 2 h + $Ta(EtO)_5$,6 h	3.8	19
$NaTaO_3$	Sol–gel synthesis,	CH_3COONa + $TaCl_5$ + citric acid,500 °C/5 h	4	20
$CaSnS_3$	Two-step ultrasonic spray	Ca + Sn + O_2 800 °C + S 500 °C/2 h	1.72	21
$LaYS_3$	Sputter-deposited precursors + vulcanization	La + Y + O_2; +S 900 °C	2	22
$BaZrS_3$	Solution deposition	Barium dithiocarboxylate species,575 °C		23

$PbTaS_3$,[96] $PbNbS_3$[97]) were prepared in this way. Other variants of this technology, such as solid-state synthesis at high pressure, have also been developed and applied (for the synthesis of $PbZrS_3$,[98] $BaSnS_3$,[99] $SrSnS_3$,[99] and $PbSnS_3$[97]). However, this often puts forward different requirements for the preparation of PSCs. First of all, these processes introduce various issues. Due to the temperature requirements of this processing method, it is often impossible to achieve such high temperatures when preparing suitable thin-film devices, which means that if this method is blindly used to process a sulfur-containing perovskite structure, the non-perovskite structure of NH_4CdCl_3/Sn_2S_3 may emerge, unless subjected to some other externalities to stabilize it.[9,13]

Secondly, the process of high-temperature treatment may be accompanied by changes in the structure of some materials and the degradation of their physical and chemical properties. A relatively common phenomenon is the lack of anionic sulfur. This may be due to the low vacancy formation energy of the S element itself, which often leads to the degradation of the perovskite structure.[88,100–102]

One of the widely used solid-state syntheses of chalcogenide perovskites is through the solid-state synthesis of oxide perovskites, followed by CS_2 vulcanization (for the synthesis of $CaZrS_3$).[7,88] However, it should be emphasized that the synthesis conditions play a fundamental role in the formability and phase determination of the required material. Vulcanization is a well-established method for synthesizing chalcogenides. Perera and colleagues observed that $BaZrO_3$ (precursor) has a grain size of about 10^2 to 2×10^2 and does not show light absorption in the visible spectrum. However, after the vulcanization process of the sample, the particles become larger (μm), showing a wide range of visible spectra (light) absorption. They also observed that the bandgap (E_g) of these materials can be easily and systematically controlled by changing the chemical concentration ratio of chalcogenide samples to prepare oxygen sulfides.[88] In fact, the sulfide structure of $Ba(Zr_XTi_{1-X})S_3$ can only be achieved by vulcanization of oxide perovskites with CS_2,[7,14] and direct synthesis by the solid-state reaction of sulfide precursors is not feasible. In contrast, $SrZrS_3$ vulcanized with CS_2 yields a non-perovskite structure,[79] while a standard solid-state reaction yields a perovskite structure.[7]

$$2BaZrO_3 + 3CS_2 \rightarrow 2BaZrS_3 + 3CO_2 \quad (3)$$

However, when comparing various synthesis methods for preparing $BaZrS_3$, a common issue with the direct synthesis of chalcogenide perovskites is the formation of unwanted products, such as binary sulfides or binary oxides.[7,15] The $BaZrS_3$ produced by the direct reaction of disulfide precursors or element precursors is more susceptible to oxidation,[92] when contrasted with the structure produced by the conversion of oxide perovskites ($BaZrO_3$) by carbon disulfide (Fig. 4c). This susceptibility to oxidation is not affected by the synthetic environment (such as a nitrogen atmosphere), but rather by the stoichiometry of elements. For chalcogenides, this can usually be achieved by providing a molten sulfur (S) phase. Wang and colleagues synthesized $BaZrS_3$ by adjusting the ratio of S in the solid-state route and achieved higher $BaZrS_3$ yield at growth temperatures as low as 600 °C.[103,104] It was mentioned that if too little excess S is added, the $BaZrS_3$ product is absent

or poorly crystalline, and the main products are BaS, BaS_2, and ZrS_2. On the other hand, if too much S is added, the main products are S-rich binary compounds BaS_3 and ZrS_3. As also mentioned by Comparotto *et al.*, unwanted phase formation is attributed to the S-rich factor.[15] However, due to the lack of information about the formation process and kinetics, it is difficult to speculate on the optimal synthesis procedure. The synthesis temperature of $BaZrS_3$ and other chalcogenides is very high, which indicates that there is a high energy barrier in the formation and nucleation of this compound, which may be responsible for its high stability. Therefore, understanding the thermodynamics and kinetics of the formation reaction is a fundamental step to optimize this material for energy applications. Recently, Kayastha and his colleagues have tried to improve the thermodynamic interpretation of the transition between 3D sulfur perovskites and 2D structures at high temperatures through a combination of experiments and calculations. Due to their similarity in Gibbs free energy, the overall S-element ratio in the synthesis process and the requirements of the synthesis environment are considered. The results suggest that chalcogenide perovskite compounds may need to master the equilibrium of the two-phase structure at low temperatures, and finally be deposited and integrated into optoelectronic devices.[10]

Ramanandan *et al.* further investigated the thermodynamic distribution and study of $BaZrO_3$ (precursor) vulcanized by H_2S. As the temperature rises, the overall structure is completely vulcanized at 1000 °C. The sensitivity of BaZrS to temperature was discussed. In practice, the formation mechanism of BaZrS is based on a two-step reaction involving (a) the intermediate amorphous phase of BaZrO, and (b) subsequently crystallized into the c$BaZrS_3$ intermediate amorphous Ba–Zr–S–O phase[93] (Fig. 4d). Ruddlesden–Popper perovskite chalcogenide $Ba_3Zr_2S_7$ was successfully synthesized by Niu *et al.* $Ba_3Zr_2S_7$ has a suitable band gap, high absorption coefficient near the absorption edge, a photoluminescence peak located at 1.28 eV, an external luminous efficiency of 0.15%, and an effective minority carrier recombination time of 65 ns, indicating that $Ba_3Zr_2S_7$ is a promising photoabsorbent for solar cells[16] (Fig. 4b). They also prepared high-quality $BaZrS_3$ and its Ruddlesden–Popper, and $Ba_3Zr_2S_7$ phase crystals by the flux growth method.[17] Subsequently, they synthesized the hexagonal perovskite chalcogenide compound $Sr_{1+x}TiS_3$ with a quasi-one-dimensional structure. The material shows a strong dichroic window and strong dichroism peak from 2.5 mm to 12 mm, with a dichroic ratio in the infrared (MWIR) region exceeding 20.[18]

3.2.2. Relatively low-temperature synthesis methods. Another method of synthesizing pure sulfur perovskite structures is through catalytic synthesis, which reduces the reaction temperature on the basis of the conventional solid-state reaction of BaS (and SrS), and Zr and sulfur (S) as catalysts in the presence of iodine. Iodine greatly increases the reaction rate of transition metals by forming volatile compounds such as low melting point iodides. Thus, compared to other synthesis methods, this method can simply homogenize TMPC ($BaZrS_3$, α-$SrZrS_3$, and β-$SrZrS_3$) in a few hours to days, while other

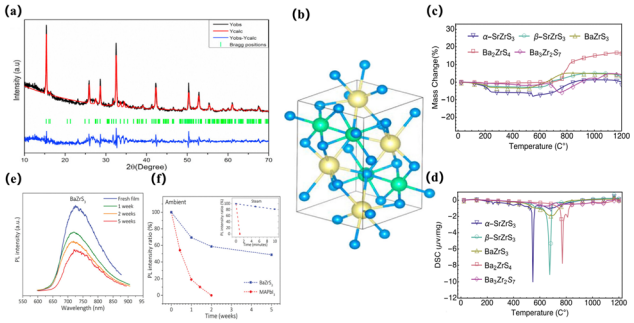

Fig. 5 Related optoelectronic performance of AMS_3 (a) Rietveld refinement of the $CaSnS_3$ X-ray diffraction pattern. (b) Side view of the structural presentation of $CaSnS_3$ lattice shaping in a distorted perovskite structure (space group Pnma). Color code: Ca $\frac{1}{4}$ yellow, Sn $\frac{1}{4}$ green, and $S\frac{1}{4}$ Blue.[21] Copyright 2021, Journal of Alloys and Compounds. (c) TGA mass change of five sulphide samples and (d) DSC change with temperature.[106] Copyright 2018, Journal of Materials Research. (e) PL spectra of $BaZrS_3$ thin films kept under ambient conditions for 5 weeks. (f) PL intensity ratios of $BaZrS_3$ and $MAPbI_3$ thin films under ambient conditions. The inset shows PL intensity ratios for steam exposure.[90] Copyright 2020, Advanced Functional Materials.

synthesis methods require weeks of repeated grinding and annealing to homogenize. Of course, compared to other "non-perovskite" structures, there are many other methods, such as the hydrothermal method and solid-state reaction.[19,20] Recently, Shaili *et al.* reported that the way of synthesizing $CaSnS_3$ by ultrasonic spray regulation at a low temperature of 500 °C, realized a diamond-shaped system similar to the P-shaped structure, and which was verified by XRD[21] (Fig. 5a and b). At present, this work appears to be the work of generating chalcogenide lattices by solid-phase vulcanization at a lower cost and simpler treatment, but it has also been partially questioned due to its XRD data and lattice constants.[105]

Of course, for optoelectronic devices, a gentle approach to structuring solar cells is the ideal solution. Ravi *et al.* prepared solution-treated films using colloidal dispersions of solid synthesized $BaZrS_3$. Chalcogenide perovskite thin-film transistors were prepared by low-temperature annealing.[92] The results show that $BaZrS_3$ nanocrystals exhibit bipolar behaviour in which hole mobility is three times higher than electron mobility, but the electrical conductivity is still very low (0.059 and 0.017 $cm^2\ V\ s^{-1}$). This may be due to the small size of the nanoparticles processed by low-temperature treatment. This is the only report of working thin-film phototransistor devices based on chalcogenide perovskites. Of course, there have been reports of photovoltaic devices based on evaporating $LaYS_3$ thin films, but the photocurrent has not yet been detected.[22] In the latest study, Pradhan *et al.* synthesized the fourth group of metal dithiocarbamates by inserting carbon disulfide into a single-phase solution and then vulcanized $BaZrS_3$ and $BaHfS_3$ after treatment at 575 °C[23] (Fig. 4f). In 2022, Jonathan and his partners used a combination of soluble barium mercaptan and nanoparticle zirconium hydride. After solution-based precursor deposition and subsequent vulcanization, $BaZrS_3$ can be obtained at temperatures as low as 500 °C[94] (Fig. 4g). However,

compared to traditional halide PSCs, these solution deposition methods often require high-temperature post-treatment or long-term annealing, which may be related to the difficulty of the crystallization structure of sulfur atoms.

But in fact, one of the main advantages of halide PSCs over monocrystalline silicon cells is the improvement of solution processing and thin film growth. Halide perovskites are usually coated with solutions of metal halides (such as PbI_2), organic cations (such as MA^+), and various additives, followed by mild heating (<250 °C), in which the solvent evaporates, and the perovskite film crystallizes. Solvents are selected for good solubility and relatively low boiling point of precursor materials. Dimethylformamide and dimethylsulfoxide are common examples. Mild heating or the addition of anti-solvent can lead to perovskite saturation and precipitation. The cationic and anionic components of halide perovskites can be provided in a single solution without the need for additional counterions. Solution growth of halide perovskites is usually carried out in a glove box to prevent degradation of perovskite products from contact with air or moisture.

In general, for chalcogenides, it is more common to grow thin films by physical vapor deposition (PVD) methods, including thermal evaporation, electron beam evaporation, and sputtering. These methods can deposit high-purity and additive-free films. Various deposition processes exist in which the elements are deposited simultaneously or sequentially, and the thermal energy required to react with them can be provided during the deposition process or subsequently in a separate heating step. Chalcogenides can be included in the deposition step, added entirely during heating, or some combination of both. Regardless of the growth order, the temperature required to form a highly crystalline material is almost always in the range of 450–600 °C. Relatively speaking, the higher synthesis temperature and relatively more difficult processing methods explain the stability of the structural bonds of the chalcogenides themselves. In general, materials with stricter crystal structure processing tend to exhibit better external stability.

In this case, some of the processes used to obtain crystalline and phase-pure materials are summarized, but these very high temperatures are another important obstacle to be overcome in perovskite optoelectronic devices. After all, a high-temperature process is not compatible with most thin-film device processes. So far, among the perovskite components we have discussed, only $BaZrS_3$ has been prepared in the form of thin films.

3.2.3. Other methods and properties. Compotto *et al.* deposited $BaZrS_3$ thin films by sputtering at room temperature, but the deposited films still require high-temperature heat treatment to improve the crystallinity of the material, but this involves a high temperature of about 900 °C, which is inconsistent with the structural design and preparation of PSCs.[15] At the same time, Wei *et al.* prepared $BaZrO_3$ films by pulsed laser deposition and obtained $BaZrS_3$ films through high-temperature vulcanization[91] (Fig. 4a). They also prepared a photodetector and evaluated the optical response and electrical behaviour of the material. They found that it has excellent N-type conductivity and good carrier mobility around 14 $cm^2 V s^{-1}$, which may be related to the lone pair electrons of sulfur vacancy. Unfortunately, the vulcanization temperature used to prepare a photodetector makes the process unsuitable for most optoelectronic devices, especially for PSCs.

It can be observed that the chalcogenide material itself is highly stable in the water and oxygen environment, can operate in higher humidity environments, and has a promising alternative structure as a perovskite solar cell. However, theoretical calculation can only simulate the properties of materials to a certain extent, and whether chalcogenide compounds are highly stable or not remains to be verified by experimental results. In 2018, Niu *et al.* studied the thermal stability of five compounds: α-$SrZrS_3$, β-$SrZrS_3$, $BaZrS_3$, Ba2ZrS_4, and $Ba_3Zr_2S_7$. They performed TGA and DSC measurements while heating the materials in air to 1200 °C. It was found that the needle-like phase of $CSrZrS_3$ first degraded at 550 °C, while the other phases appeared to be fairly stable in air, and their oxidative decomposition temperature was much higher than 600 °C. Mass changes and post-XRD analysis confirmed this. It has also been reported that long-term ambient air storage and repeated water washing have no effect on the properties observed by XRD or UV-vis spectrophotometry of $BaZrS_3$[106] (Fig. 5c and d). Similarly, the stability of lead-free chalcogenide perovskite $BaZrS_3$ films was also demonstrated by Gupta *et al.*, who compared the properties of $BaZrS_3$ and $MAPbI_3$ in terms of moisture retention and light-induced degradation. $BaZrS_3$ is more stable than methylammonium lead iodide ($MAPbI_3$) in humid environments due to its weaker interaction with water and very low ion mobility. Under identical environmental conditions, the light response of the $BaZrS_3$ device remained at 60% of its initial value after 4 weeks, while the light response of the $MAPbI_3$ device decreased by 95% after a mere 4 days[90] (Fig. 5e and f). In addition, in 2023, Zhang *et al.* discovered that $LaScSe_3$ is a thermodynamically stable selenide perovskite through the first principles calculation and accurate prediction of phase stability standard, and successfully verified this in subsequent experimental synthesis.[107]

In general, the currently commonly used methods for pure sulfur-structured sulfides are often achieved by using alkaline earth metals and group IV transition metals or thiourea salt. Additionally, coating or heat treatment with thiourea is often employed, requiring constant temperature and humidity in the controlled environment.[108] Of course, this is only required during preparation, and films tend to show ultra-long stability after preparation. Another way to circumvent the instability of precursor materials is to deliberately deposit an oxide film and then convert to chalcogenides by heat treatment with an S(e) source. Nevertheless, the exceptional stability of sulfides and their potential as light harvesters remain the primary advantages of thin-film solar cells. Challenges such as the requirement for high growth temperatures, slow crystallization, and compatibility issues with conductive substrates all arise from the same root issue. The use of oxide precursors presents inherent difficulties in removing oxygen, and attempts to crystallize directly from amorphous precursor membranes fail due to (possibly) slow diffusion kinetics. Unfortunately, owing

to the current process requirements and limitations of processing methods, researchers have not been able to fabricate devices with an ultra-high PCE of more than 26% in this way. Therefore, the question of how to improve the performance of the device or enhance its ability to generate photogenerated carriers as a solar light harvester is a very important area of research. The improvement of its device manufacturing process is also a major research direction, especially the current relatively mild improvement method also requires an environment of about 200 °C. Finally, in order to improve its performance, the researchers adopted another method to improve its performance, that is, halides are introduced into the chalcogenide structure to prepare a light-absorbing layer with a "perovskite-like" structure.

4. Solar cells with a chalcogenide-halide blend structure

Considering the high efficiency of halide PSCs and the long-term water-oxygen stability of chalcogenide perovskite structures, the researchers tried to combine halides and chalcogenides, and gradually introduced a large number of halogen anions into the synthesis of chalcogenide compounds. Many chalcohalide crystal materials with a "perovskite-like" structure were synthesized. This type of solar cell structure combines the advantages of halide-soluble processing with long-term stability requirements (Table 2).

4.1. One-stage method

By replacing the ions in the perovskite with some sulfur-containing structural ions, this method aims to improve the crystallization properties and surface morphology of the perovskite structure and achieve the effect of improving the structural stability. In 2017, Kaltzoglou *et al.* prepared halide PSCs at room temperature by introducing trimethylthiotriiodide, which exhibits high chemical stability in the environment. Compared to protonated amine cations, $(CH_3)_3S$ has no hydrolysis reaction and shows no signs of degradation in air up to 85 °C. But in contrast, methylamine in PSCs is replaced by trimethylsulfide molecules, and the feasibility of replacing methylamine with trimethylsulfide ions is proposed. This is also the first report on the lead sulfide perovskite compound[109] (Fig. 6e). In 2022, Ming and his colleagues explored stable, lead-free, and defect-resistant photovoltaic materials. They combined computational screening with experimental synthesis, utilizing large cations with a single pair of electrons and mixed anions of sulfur and halogens as the marker structure, while achieving defect tolerance and high stability. Combining the criteria with direct bandgap and optimal bandgap values, the screening of the inorganic materials database identified $CuBiSCl_2$ with an ideal bandgap of 1.37 eV in the perovskite structure. Experiments have found that the material remains stable under thermal decomposition at 300 °C and can be stored for 25 days under environmental conditions with a relative humidity of 60%. A prototype of the solar cell was made, proving that the open-circuit voltage is 1.09 V and the PCE is 1.00%[34] (Fig. 6d).

Tiwari *et al.* applied spin coating technology to the one-step preparation of BiSI thin films.[35] They spin-coated with a molecular solution synthesized by dissolving $Bi(NO_3)_2{\cdot}_5H_2O$, thiourea, and NH_4I in a mixture of 2-methoxyethanol and acetylacetone. Using this method, flake BiSI films are produced. Similarly, Nishikudo *et al.* reported that the $Sb(EtX)_3$ single crystal was used for spin coating based on the one-step method. To make SbSI solar cells, the solution of the $Sb(EtI)_3$ single crystal and SbI_3 dissolved in dimethyl sulfoxide was spun onto the substrate of the mesoporous TiO_2 (mp-TiO_2)/TiO_2 barrier (TiO_2-BL)/FTO and annealed at 240 °C. Then, HTL and Au are deposited[36] (Fig. 6f). In 2019, Yao and colleagues used the developed low-pressure vapor-assisted solution process (LP-VASP) method to obtain sulfur-doped bismuth-based perovskite films. Due to the presence of sulfur, the crystal quality and band properties were effectively improved in the prepared lead-free perovskite thin films. Through systematic study of the effect of reaction time on device performance, it is found that the optimized reaction time is 30 min, at which time the bandgap of the sulfur-doped $MA_3Bi_2I_{9-2x}S_x$ perovskite film decreased to 1.67 eV, and the morphology is compact. The corresponding optimal PCE reaches 0.152%. This study provides a new method for incorporating sulfur into lead-free bismuth PSCs[37] (Fig. 6b). In addition to ternary MChX, the one-step spin coating method can also be used to prepare quaternary sulfur halide ($M_{II2}M_{III}Ch_2X_3$).

4.2. Two-stage method

In the two-step deposition method, sulfide (M_2CH_3) is prepared and then converted to chalcohalides (MChX) by the reaction of M_2CH_3 and MX_3 (step 2). This inverse application eqn (4) says.

$$M_2Ch_3 + MX_3 \rightarrow 3MChX \quad (4)$$

The most systematic and impactful work in this area is the related research of Nie and colleagues. The $Pb_2SbS_2I_3$ material was synthesized based on an early report from Starosta *et al.* The stoichiometric elements Sb, Pb, S were weighed in quartz glass ampoules and reacted with sublimed iodine in a furnace at 650 °C for 36 h. The synthesized $Pb_2SbS_2I_3$ material shows a bandgap of 2.0 eV.[111] In 2018, Nie *et al.* prepared films by chemical bath deposition (CBD) of Sb_2S_3 films and SbI_3 solution in *N*-dimethylformamide (DMF) in argon or nitrogen.[38] A combination of solution treatment and solid state reaction prepares SbSI thin films. SbSI-based solar cells were fabricated by fluorine-doped SnO_2 (FTO)/TiO_2 resistance tomography (BL-TiO_2)/mesoporous TiO_2 (mp-TiO_2)/SbSI/hole transport material (HTM)/Au cell structure[39] (Fig. 7a–d). This protocol is also applied to prepare solar cells with an $MASbSI_2$ structure and $Pb_2SbS_2I_3$ as a light harvester, respectively. $Pb_2SbS_2I_3$ solar cells without encapsulated nanostructures show good humidity stability within 30 days, and the effect of PbI_2 solution concentration on device performance was studied. The role of trap states is studied to elucidate the potential

Table 2 Summarized reports of "perovskite-like" cells in different energy device applications

Material	Reaction conditions	Band gap(eV)	Device structure/measurement conditions	Performance	Ref.
$CuBiSCl_2$	CuCl + $BiCl_3$ + Bi_2S_3 ground and pressed into tablets. The quartz tube was put into a box furnace, which was ramped to 430 °C within 10 h, dwelled for 10 h, cooled down to 200 °C within 60 h.	1.37	FTO/BL-TiO_2/mp-TiO_2/$CuBiSCl_2$/Sn	J_{SC} = 1.38 mA cm^{-2} V_{OC} = 1.09 V FF = 0.66 PCE = 1.00%	34
BiSI	$Bi(NO_3)_3$ + thiourea + NH_4I in 2-methoxyethanol: acetylacetone (4 : 1 v/v); heating at 200 °C in the air for 5 min.	1.57	FTO/SnO_2/BiSI/F8/Au	J_{SC} = 8.44 mA cm^{-2} V_{OC} = 0.445 V FF = 0.3514 PCE = 1.32%	35
Sb_2S_3-containing SbSI	Spin-coating method using metal ethylxanthate as the metal and sulfur source for the preparation of MSX and SAP thin films.	—	FTO/compact-TiO_2/mp-TiO_2/SbSI/PCPDTBT/PEDOT: PSS/Au	J_{SC} = 12 mA cm^{-2} V_{OC} = 0.47 V FF = 0.52 PCE = 2.91%	36
$(CH_3NH_3)_3Bi_2I_9$	Bi(xt)$_3$ (xt = ethyl xanthate) precursor solution was spin-coated on the substrate and then the samples were put in a covered Petri dish at 10 kPa with MAI powder scattered around uniformly. The sulfur incorporated MBI film was prepared at 150 °C with the different reaction times.	2.1	FTO/BL-TiO_2/mp-TiO2/$MA_3Bi_2I_9$/spiro-OMeTAD/Au	J_{SC} = 0.58 mA cm^{-2} V_{OC} = 0.54 V FF = 0.472 PCE = 0.152%	37
Sb_2S_3-SbSI	In the solution process, SbSI is prepared by multiple cycles of spin-coating of the SbI_3 solution onto the FTO/BL/mp-TiO_2/Sb_2S_3 sample and thermal annealing. In the vapor process, SbSI is formed by simply annealing the FTO/BL/mp-TiO_2/Sb_2S_3 sample and SbI_3 powder (which vaporizes under the annealing condition) together.	—	FTO/TiO_2-BL/mp-TiO_2/Sb_2S_3-SbSI/PEDOT: PSS/Au	J_{SC} = 14.31 mA cm^{-2} V_{OC} = 0.55 V FF = 0.661 PCE = 5.38%	38
SbSI	1. Sb_2S_3: sodium thiosulfate in water + $SbCl_3$ in acetone +water: reaction at 10 °C, followed by annealing in Ar at 300 °C for 5 min. 2. SbSI: SbI_3 in DMF spin coated on Sb_2S_3, followed by annealing at 150 °C for 5 min in an inert atmosphere.	2.15	FTO/BL-TiO_2/mp-TiO_2/SbSI/PCPDTBT/Au	J_{SC} = 9.11 mA cm^{-2} V_{OC} = 0.58 V FF = 0.577 PCE = 3.05%	39
$Pb_2SbS_2I_3$	1. Sb_2S_3: sodium thiosulfate in water + $SbCl_3$ in acetone + water: reaction at 10 °C, + annealing in Ar at 300 °C for 5 min. 2. SbSI: SbI_3 in DMF spin coated at 500–2000 rpm for 60 s on Sb_2S_3, annealing in Ar at 300 °C for 2 min.	2.19	FTO/BL-TiO_2/mp-TiO_2/$Pb_2SbS_2I_3$/PCPDTBT/Au	J_{SC} = 8.79 mA cm^{-2} V_{OC} = 0.61 V FF = 0.582 PCE = 3.12%	40
SbSI	1. Sb_2S_3: $SbCl_3$, + thiourea in DMF spin-coated, followed by heat treatment at 150 °C for 5 min inside a glovebox. 2. SbSI: Spin coating of SbI_3 in NMP/DMSO solution on Sb_2S_3, followed by annealing at ~200 °C for 1 h.	1.96	FTO/TiO_2/SbSI/P3HT/Au	J_{SC} = 5.45 mA cm^{-2} V_{OC} = 0.548 V FF = 0.31 PCE = 0.93%	41
$Sb_{0.67}Bi_{0.33}SI$	1.Sb_2S_3: sodium thiosulfate in water + $SbCl_3$ in acetone + water, reaction at 10 °C, followed by annealing in Ar at 300 °C for 5 min. 2. $Sb_{0.67}Bi_{0.33}SI$: BiI_3 in DMF spin coated on Sb_2S_3, followed by annealing at 200 °C for 2 min in an inert atmosphere.	1.62	FTO/BL-TiO_2/mp-TiO_2/SbSI/PCPDTBT/Au	J_{SC} = 14.54 mA cm^{-2} V_{OC} = 0.53 V FF = 0.528 PCE = 4.07%	42
$Pb_3S_2X_2$ (X = Cl, Br, I)	PbX_2 (X = Cl, Br, I) and Pb $(SCN)_2$ in ODE + OLA + OA, reaction at 130 to 170 °C for 1 h.	1.76 ($Pb_3S_2I_2$) 1.98 ($Pb_3S_2Br_2$) 2.02 ($Pb_3S_2Cl_2$)	ITO/AZO/$Pb_3S_2Br_2$/MoO_X/Au	J_{SC} = 1.2 mA cm^{-2} V_{OC} = 0.57 V PCE = 0.21%	43

mechanism of different reorganization processes. Based on their previous optimization work, such as spin-coating conditions, m-TiO_2 thickness, and Sb_2S_3 deposition time, the PCE is approximately 3.12%, J_{SC} is 8.79 mA cm^{-2}, V_{OC} is 0.61 V, and FF is 58.2%. An optimized crystal structure of the synthesized $MASbSI_2$ perovskite was prepared, with sulfur atoms distributed along the *Z* axis of the octahedral unit. The Sb–S bond is divided into a long bond (long bond) and a short bond (short bond). The length of the Sb–I bond is 3.16 Å. As a whole, it shows a strict cubic structure. This explains the impressive stability of sulfur halide materials compared to lead halide perovskite materials[40,78] (Fig. 7e–f). An optimized crystal structure of the synthesized $MASbSI_2$ perovskite was prepared, with sulfur atoms distributed along the *Z*-axis of the octahedral unit. The Sb–S bond is divided into a long bond (~3.6 Å) and a short bond (~2.27 Å). This series of processing methods for preparing chalcogenide solar cells is also applied to selenium-based structures, and the PCE(PCE) is 4.1% under standard air mass. Even if illuminated at AM1.5G (100 mW cm^{-2}) for the 2321 min, the device retains 90.0% of the initial PCE.[112] In addition, Zhang *et al.* first prepared $MABiI_2S$ perovskite structure crystals by a two-step solid-state synthesis method, showing high crystallinity overall[110] (Fig. 6a). Choi *et al.* reported a simple two-step solution treatment method based on the

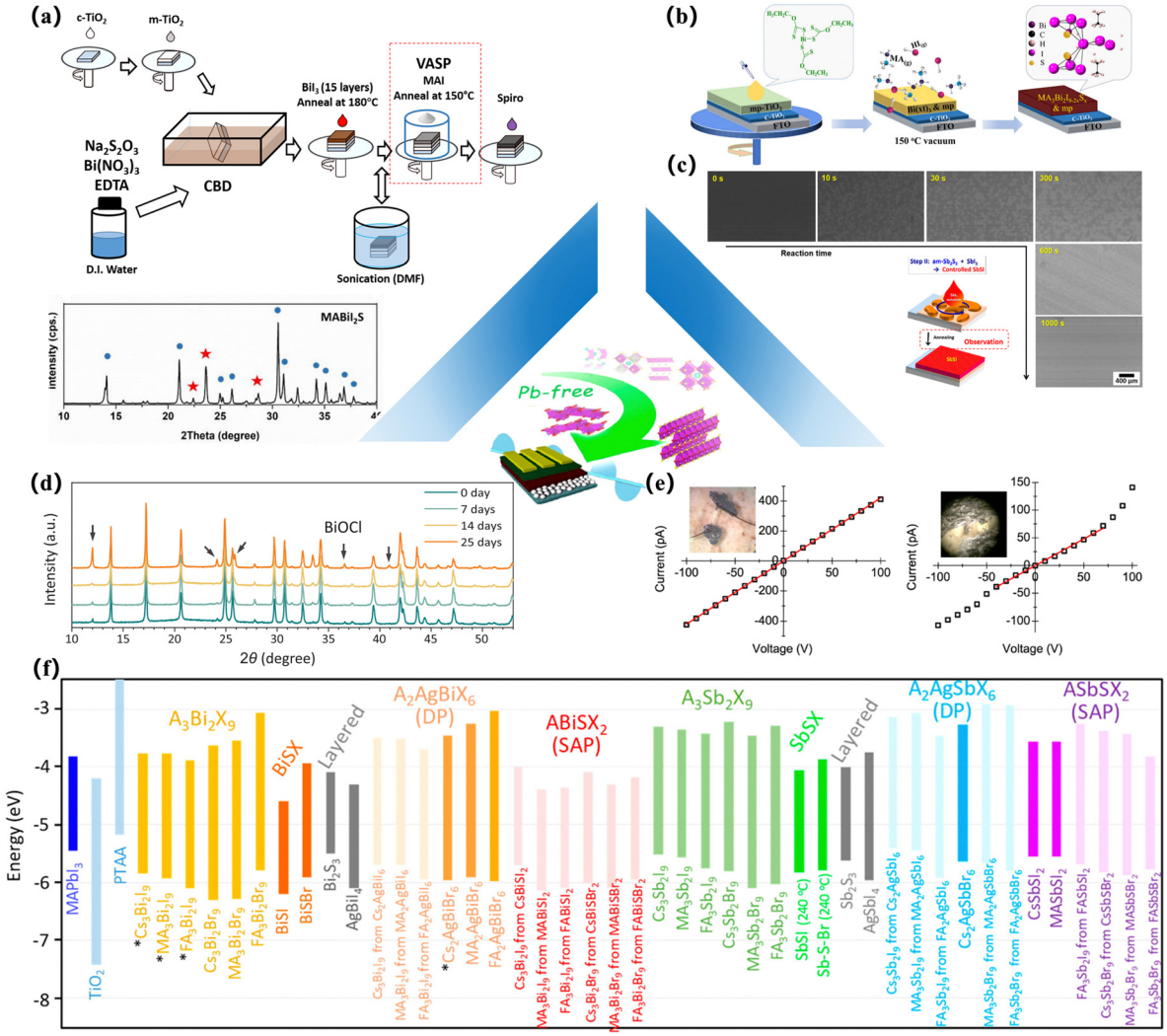

Fig. 6 Preparation of some chalcogenide perovskite-like thin film devices. (a) The solid-state synthesis procedure of the MBIS perovskite for the device fabrication process.[110] (b) A schematic illustration of the fabrication process of S-incorporated bismuth-based perovskites solar cells *via* low-pressure vapor-assisted solution process (LP-VASP).[37] Copyright 2019, Solar RRL. (c) FESEM images of the samples obtained at different reaction times; Typical FESEM surface image around a dot.[41] Copyright 2018, APL Materials. (d) Evolution of XRD patterns for the $CuBiSCl_2$ samples stored at room temperature in air with 60% relative humidity. The black arrows mark the peaks attributed to the compound BiOCl.[34] Copyright 2022, Advanced Functional Materials. (e) *I*–*V* plot for single crystals of $(CH_3)_3SPbI_3$ at room temperature. Needle-shaped crystal from a DMF solution with dimensions (inset) 0.2 mm × 0.2 mm × 1.3 mm, and plate-like crystal from an HI solution with dimensions (inset) 0.1 mm × 0.1 mm × 0.03 mm. The former crystal exhibits a regular ohmic behavior in the ±100 V range, whereas the latter shows signs of polarization above ±50 V.[109] Copyright 2017, Inorganic Chemistry. (f) Energy levels of the VBM and CBM for the direct transitions of the Bi- and Sb-based films.[36] Copyright 2020, Chem Mater.

formation of amorphous Sb_2S_3 (am-Sb_2S_3) using the $SbCl_3$-TU solution in step I and the application of SbI_3 to am-Sb_2S_3 in step II to obtain the final SbSI film. In addition, the structure and morphology of the final SbSI film can be controlled by high-concentration treatment, and a dense SbSI film with a pure SbSI phase can be obtained at a low temperature of 200 °C. The successful application of the SbSI thin film to planar SbSI solar cells demonstrates the controlled growth of the SbSI thin film and its application in planar solar cells for the first time[41] (Fig. 6c).

However, in practice, it is found that the Sb_2S_3 structural lattice will cause lattice distortion, which further affects the trap density and photovoltaic performance, insufficient light absorption and charge transfer, or the device efficiency will be reduced if the concentration of the $SbCl_3$ precursor solution is too low or too high.

The poor efficiency of the device (in high concentrations of $SbCl_3$ precursor solutions) is mainly due to the high trap density and deep-level trap state. It is worth noting that the unpackaged device exhibits excellent thermal stability, light stability, and long-term stability when stored for 504 h, which indicates that $Sn_2SbS_2I_3$ materials have higher stability than Sn-based halide perovskites. In 2019, Nie *et al.* deposited Sb_2S_3 on the FTO/TiO_2-BL/mp-TiO_2 substrate, and Sb_2S_3 was replaced and modified by Bi and I ions. After deposition of amorphous Sb_2S_3 and annealing, the solution of BiI_3 in DMF is spin-coated

on FTO/TiO_2-BL/mp-TiO_2/Sb_2S_3. The sample was annealed in argon or nitrogen at 250 °C, and the process was repeated several times until Sb_2S_3 was fully converted to $Sb_{0.67}Bi_{0.33}SI$[42] (Fig. 7g and h).

However, these methods are time-consuming because they require multiple cycles in step 2 to obtain complete thioiodide. In addition, the film obtained is not entirely homogeneous. To overcome these limitations, we introduced the SbI_3 vapor process instead of the SbI_3 solution process in step 2, in order to produce higher SbSI uniformity without repeating step 2 and provide a better 3.62% PCE for SbSI solar cells. However, the inherent limitations of the CBD process, such as the formation of impurities and difficulties in controlling the proportions, may limit the controlled growth of sulfur halides.[114] In addition, since the structure of mesoporous devices is optimized, factors such as morphology and thickness, which are important for planar devices, are not considered. Therefore, developing a two-step method for planar device architectures that allows for controlled growth of sulfur halide remains a challenge.

To apply a two-step approach to the planar device architecture, a thin film covering the entire surface is required. This is because incomplete surface coverage reduces the ability to absorb light and produces defects, which reduces the performance of the device.[115] Recently, Xiong *et al.* presented their own views and reported a method for preparing BiSI nanorod arrays based on the two-step method. However, their method

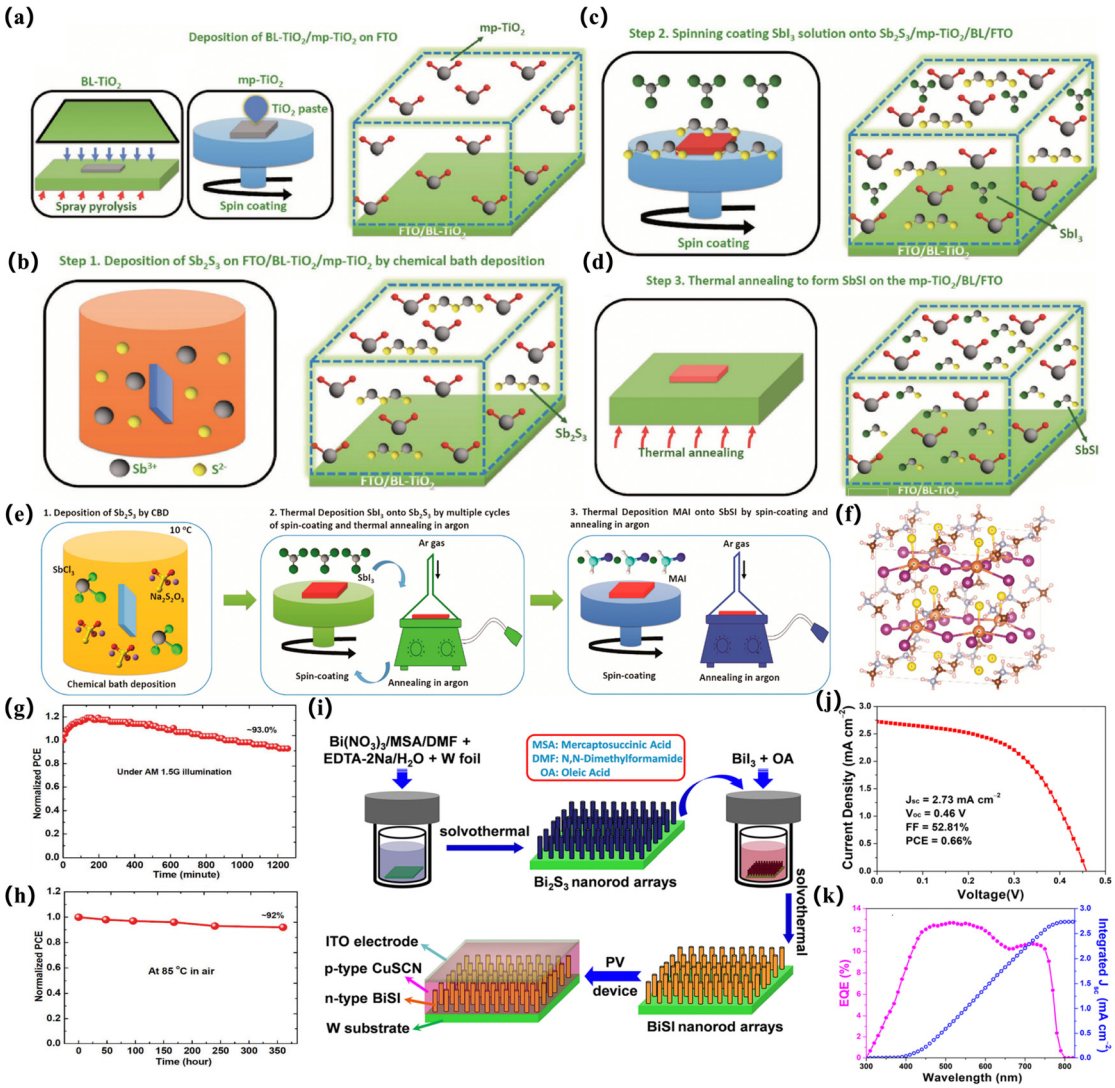

Fig. 7 Preparation of some sulfur "perovskite-like" solar cell devices. (a)–(d) Schematic illustration for preparing SbSI layers through the reaction between Sb_2S_3 deposited by the CBD process and SbI_3 onto mp-TiO_2 electrode.[39] Copyright 2017, Advanced Energy Materials. (e) Process for preparing the $MASbSI_2$ perovskite layer, (f) $MASbSI_2$ configuration simulated by DFT calculation is presented by the ball and stick model with the orange ball for Sb, purple for I, yellow for S, gray for C, brown for N, and white for H.[78] Copyright 2018, J Am Chem Soc. (g) under standard AM 1.5G illumination with a xenon lamp including UV radiation at room temperature and (h) measured at 85 °C in air, under 40% average relative humidity in the dark.[42] Copyright 2019, Advanced Materials. (i) Schematic illustration of the growth procedures of BiSI nanorod arrays and their application for solar cells (j) Typical *J*–*V* curve of the ITO/p-CuSCN/n-BiSI/W solar-cell device based on BiSI nanorod arrays. (k) EQE spectrum and the corresponding integrated J_{SC} of the fabricated solar cell device.[113] Copyright 2020, ACS Sustain Chem Eng.

involves solvothermal synthesis rather than spin coating at each step. Bi_2S_3 deposited tungsten (W) foil is immersed in an autoclave containing BiI_3 solution, and BiSI nanorods are prepared by heating. Compared with the two-step method, the prepared nanorods have an E_g value similar to 1.57 eV but show a preferred [010] orientation[113] (Fig. 7i–k).

4.3 Other methods

In addition to the methods mentioned above for preparing solar cells, there are other methods for the processing and modification of solar cells. Manna *et al.* have developed a colloid synthesis method for the synthesis of $Pb_4S_3X_2$ (X = Cl, Br, and I) NC, which has made further progress in the synthesis of Pb-based sulfur halides. A heating method has been developed in which hot thiocyanate (SCN^-) ions (as a source of S^{2-}) decompose at lower temperatures (below 190 °C) in the presence of corresponding $PbBr_2$, PbI_2, $PbCl_2$ precursors and OLA and OA solvents.[43] The energy arrangement on $Pb_4S_3Br_2$ NC after ligand exchange was studied to test its applicability in the fabrication of solar cells. Unencapsulated solar cells configured with ITO/AZO/$Pb_4S_3Br_2$/MoO_X/Au have a PCE of 0.21 ± 0.02% under standard AM 1.5G illumination, a J_{SC} of 1.09 mA cm^{-2}, and a V_{OC} of 0.58 V. Kunioku *et al.* heated BiOI particles in H_2S or H_2Se gas for a short time <1 h. By replacing O^{2-} with S^{2-}, $Bi_SBr_{1-X}I_X$ was also synthesized by this low-temperature anion substitution, and the composition ratio between Br and I is retained, which is attributed to the successful inhibition of halogen volatilization at such low temperatures.[116] Li fabricated a new type of ternary Bi chalcohalide, the tetragonal $Bi_{13}S_{18}I_2$, in addition to BiSI, with both controlled by adjusting the mole ratio of CH_4N_2S/BiI_3/CH_3NH_3I(CH_3NH_3I = MAI) in the solution used in the solvothermal process. They found that a pure $Bi_{13}S_{18}I_2$ structure can be obtained from the conversion reaction of BiSI over 6 h at a CH_4N_2S/BiI_3/MAI ratio of 4 : 2 : 3.[117] Kanatzidis *et al.* re-examined Sn-based sulfur iodide and demonstrated the synthesis of novel quaternary $Sn_2BiS_2I_3$ and Sn_2BiSI_5 materials using isothermal heating and chemical vapor transport. Interestingly, these compounds are stable in water and air with a band gap of 1.2–1.3 eV, which makes them promising for solar energy conversion applications. However, practical applications have not yet been proven.[118] The specific process and results of Nie *et al.* are described above, and the excellent performance of these solar cells in terms of humidity, thermal, and light stability is shown. This study is of great significance for developing and applying solar cells.

5. Summary and perspective

In summary, we have proposed various strategies for augmenting the inherent stability of perovskite materials by combining chalcogenides and halides. Introducing chalcogenides into halide PSCs has shown considerable enhancement in device efficiency and stability. A crucial aspect of research involves the incorporation of sulfur into the hole transport layer of PSCs, significantly improving long-term stability through dipole moment interactions between the lone pair electrons in chalcogenides (*e.g.*, sulfur S, oxygen O) and unpaired Pb^{2+} ions in perovskites. Additionally, integrating chalcogenides into the perovskite layer promotes crystallization properties and stability, notably through the inclusion of additives such as S_8, dithizone, and Lewis bases into perovskites. Furthermore, interface modifications employing chalcogenides have been explored in halide PSCs, including surface treatments on materials like SnO_2, NiO, and perovskites. Various methods such as solid-state reaction, vulcanization processes, and high-temperature, high-pressure synthesis are commonly used in the synthesis of chalcogenide perovskites. Catalytic synthesis, lowering reaction temperatures, has shown promise in creating pure sulfur perovskite structures. Additionally, techniques such as sputtering and pulsed laser deposition have been proposed for synthesizing chalcogenide perovskites. Despite theoretical possibilities for chalcogenide perovskites in inorganic thin film solar cells, only a limited number of stable compositions crystallize into the desired perovskite structure. Therefore, experimental research has focused on high-temperature synthesis methods and alternative catalyst-based approaches. Regarding solar cells utilizing a chalcogenide-halide blend structure, combining the high efficiency of halide perovskite solar cells with the long-term stability of chalcogenide perovskites has been explored. One-stage and two-stage methods have been employed for the preparation of mixed chalcogenide and halide perovskites. While the one-stage method offers convenience, temperature control becomes crucial due to the differing requirements of chalcogenides and halides. The two-stage method involves depositing chalcogenide at high temperatures followed by halide deposition at lower temperatures, albeit increasing preparation complexity. Moreover, various synthesis methods such as colloid synthesis, low-temperature anion substitution, solvothermal processes, isothermal heating, and chemical vapor transport have been utilized for mixed chalcogenide and halide perovskite synthesis. Despite advancements in utilizing chalcogenides to enhance solar cell stability, certain limitations persist, necessitating further research. To address these limitations, suggestions for future research can be categorized as follows:

For halide PSCs:

(a) Further optimization of perovskite structures through lead ion substitution, anion modification, and the use of non-halide anions.

(b) Incorporation of quantum dot perovskites into antisolvents for enhanced crystallization during cell preparation.

(c) Exploration of perovskite-silicon tandem solar cell structures to bolster overall stability.

(d) Utilizing virtual modelling to understand degradation mechanisms at the atomic scale, particularly regarding material properties.

For more stable chalcogenide thin film materials:

(a) Detailed theoretical calculations to identify materials suitable for solar cells.

(b) Reduction of chalcogenide perovskite synthesis temperatures to suit substrate materials.

(c) Optimization of preparation processes, including device structure and crystallization orientation regulation.

For chalcogenide-halide compounds:

(a) Discovery and development of new chalcogenide-halide materials with improved optoelectronic performance.

(b) Investigation into the intrinsic properties of chalcogenide-halide compounds and their impact on solar cell efficiency.

(c) Exploration of growth regulation techniques for enhanced performance.

(d) In-depth study of crystallization mechanisms and electronic properties of chalcogenide-halide compounds.

In conclusion, leveraging chalcogenide-halide combinations to enhance the intrinsic stability of PSCs presents a promising avenue for future research. This approach could substantially contribute to the commercialization of perovskite-based devices by broadening the scope of stability-related studies.

Conflicts of interest

The authors declare no conflict of interest.

Acknowledgements

This work was supported by financial support from the National Natural Science Foundation of China (52203359), the National Key Research and Development Program of China (2019YFA0705400), the Natural Science Foundation of China (52073119, 21774040, and 22002162), the Natural Science Foundation of Jiangsu Province (BK20212008), the Research Fund of State Key Laboratory of Mechanics and Control of Mechanical Structures (MCMS-I-0421K01), the Fundamental Research Funds for the Central Universities (NJ2020003, NZ2020001), and a project funded by the Priority Academic Program Development of Jiangsu Higher Education Institutions. R.N. and S.I.S. acknowledge financial support from the Basic Science Research Program (NRF-2018R1A3B1052820) through the National Research Foundation of Korea (NRF) funded by the Ministry of Science, ICT & Future Planning (MSIP). The research work was also supported by the supporting funds for talents of Nanjing University of Aeronautics and Astronautics.

Notes and references

1 A. Kojima, K. Teshima, Y. Shirai and T. Miyasaka, *J. Am. Chem. Soc.*, 2009, **131**, 6050–6051.
2 J. A. Brehm, J. W. Bennett, M. R. Schoenberg, I. Grinberg and A. M. Rappe, *J. Chem. Phys.*, 2014, **140**, 224703.
3 M. S. G. Hamed and G. T. Mola, *Crit. Rev. Solid State*, 2020, **45**, 85–112.
4 N. J. Jeon, J. H. Noh, Y. C. Kim, W. S. Yang, S. Ryu and S. I. Seok, *Nat. Mater.*, 2014, **13**, 897–903.
5 Best Research-Cell Efficiency Chart, **https://www.nrel.gov/pv/assets/pdfs/best-research-cell-efficiencies.pdf**.
6 S. Niu, H. Huyan, Y. Liu, M. Yeung, K. Ye, L. Blankemeier, T. Orvis, D. Sarkar, D. J. Singh, R. Kapadia and J. Ravichandran, *Adv. Mater.*, 2017, **29**, 1604733.
7 Y. Nishigaki, T. Nagai, M. Nishiwaki, T. Aizawa, M. Kozawa, K. Hanzawa, Y. Kato, H. Sai, H. Hiramatsu, H. Hosono and H. Fujiwara, *Sol. RRL*, 2020, **4**, 1900555.
8 K. Mitchell, R. C. Somers, F. Q. Huang and J. A. Ibers, *J. Solid State Chem.*, 2004, **177**, 709–713.
9 C.-S. Lee, K. M. Kleinke and H. Kleinke, *Solid State Sci.*, 2005, **7**, 1049–1054.
10 P. Kayastha, D. Tiwari, A. Holland, O. S. Hutter, K. Durose, L. D. Whalley and G. Longo, *Sol. RRL*, 2023, **7**, 2201078.
11 W. Meng, B. Saparov, F. Hong, J. Wang, D. B. Mitzi and Y. Yan, *Chem. Mater.*, 2016, **28**, 821–829.
12 K. Hanzawa, S. Iimura, H. Hiramatsu and H. Hosono, *J. Am. Chem. Soc.*, 2019, **141**, 5343–5349.
13 S.-P. Guo, Y. Chi, J.-P. Zou and H.-G. Xue, *New J. Chem.*, 2016, **40**, 10219–10226.
14 X. Wei, H. Hui, S. Perera, A. Sheng, D. F. Watson, Y.-Y. Sun, Q. Jia, S. Zhang and H. Zeng, *ACS Omega*, 2020, **5**, 18579–18583.
15 C. Comparotto, A. Davydova, T. Ericson, L. Riekehr, M. V. Moro, T. Kubart and J. Scragg, *ACS Appl. Energy Mater.*, 2020, **3**, 2762–2770.
16 S. Niu, D. Sarkar, K. Williams, Y. Zhou, Y. Li, E. Bianco, H. Huyan, S. B. Cronin, M. E. McConney, R. Haiges, R. Jaramillo, D. J. Singh, W. A. Tisdale, R. Kapadia and J. Ravichandran, *Chem. Mater.*, 2018, **30**, 4882–4886.
17 S. Niu, B. Zhao, K. Ye, E. Bianco, J. Zhou, M. E. McConney, C. Settens, R. Haiges, R. Jaramillo and J. Ravichandran, *J. Mater. Res.*, 2019, **34**, 3819–3826.
18 S. Niu, H. Zhao, Y. Zhou, H. Huyan, B. Zhao, J. Wu, S. B. Cronin, H. Wang and J. Ravichandran, *Chem. Mater.*, 2018, **30**, 4897–4901.
19 O. Vázquez-Cuchillo, A. Manzo-Robledo, R. Zanella, N. Elizondo-Villareal and A. Cruz-López, *Ultrason. Sonochem.*, 2013, **20**, 498–501.
20 W.-H. Lin, C. Cheng, C.-C. Hu and H. Teng, *Appl. Phys. Lett.*, 2006, **89**, 211904.
21 H. Shaili, M. Beraich, A. Elhat, M. Ouafi, E. Salmani, R. Essajai, W. Battal, M. Rouchdi, M. Taibi, N. Hassanain and A. Mzerd, *J. Alloys Compd.*, 2021, **851**, 156790.
22 A. Crovetto, R. Nielsen, M. Pandey, L. Watts, J. G. Labram, M. Geisler, N. Stenger, K. W. Jacobsen, O. Hansen, B. Seger, I. Chorkendorff and P. C. K. Vesborg, *Chem. Mater.*, 2019, **31**, 3359–3369.
23 A. A. Pradhan, M. C. Uible, S. Agarwal, J. W. Turnley, S. Khandelwal, J. M. Peterson, D. D. Blach, R. N. Swope, L. Huang, S. C. Bart and R. Agrawal, *Angew. Chem., Int. Ed.*, 2023, **62**, e202301049.
24 H. Min, D. Y. Lee, J. Kim, G. Kim, K. S. Lee, J. Kim, M. J. Paik, Y. K. Kim, K. S. Kim, M. G. Kim, T. J. Shin and S. I. Seok, *Nature*, 2021, **598**, 444–450.
25 Q. Jiang, J. Tong, Y. Xian, R. A. Kerner, S. P. Dunfield, C. Xiao, R. A. Scheidt, D. Kuciauskas, X. Wang, M. P. Hautzinger, R. Tirawat, M. C. Beard, D. P. Fenning,

J. J. Berry, B. W. Larson, Y. Yan and K. Zhu, *Nature*, 2022, **611**, 278–283.
26 Y. Zhao, F. Ma, Z. Qu, S. Yu, T. Shen, H.-X. Deng, X. Chu, X. Peng, Y. Yuan, X. Zhang and J. You, *Science*, 2022, **377**, 531–534.
27 E. A. Duijnstee, B. M. Gallant, P. Holzhey, D. J. Kubicki, S. Collavini, B. K. Sturdza, H. C. Sansom, J. Smith, M. J. Gutmann, S. Saha, M. Gedda, M. I. Nugraha, M. Kober-Czerny, C. Xia, A. D. Wright, Y.-H. Lin, A. J. Ramadan, A. Matzen, E. Y.-H. Hung, S. Seo, S. Zhou, J. Lim, T. D. Anthopoulos, M. R. Filip, M. B. Johnston, R. J. Nicholas, J. L. Delgado and H. J. Snaith, *J. Am. Chem. Soc.*, 2023, **145**, 10275–10284.
28 M. A. Green, A. Ho-Baillie and H. J. Snaith, *Nat. Photonics*, 2014, **8**, 506–514.
29 S. D. Stranks and H. J. Snaith, *Nat. Nanotechnol.*, 2015, **10**, 391–402.
30 J.-P. Correa-Baena, M. Saliba, T. Buonassisi, M. Grätzel, A. Abate, W. Tress and A. Hagfeldt, *Science*, 2017, **358**, 739–744.
31 Q. A. Akkerman, G. Rainò, M. V. Kovalenko and L. Manna, *Nat. Mater.*, 2018, **17**, 394–405.
32 H. J. Snaith, *Nat. Mater.*, 2018, **17**, 372–376.
33 A. K. Jena, A. Kulkarni and T. Miyasaka, *Chem. Rev.*, 2019, **119**, 3036–3103.
34 C. Ming, Z. Chen, F. Zhang, S. Gong, X. Wu, J. Jiang, T. Ye, Q. Xu, K. Yang, L. Wang, X. Cao, S. Yang, S. Zhang, Y. Zhang, J. Shi and Y.-Y. Sun, *Adv. Funct. Mater.*, 2022, **32**, 2112682.
35 D. Tiwari, F. Cardoso-Delgado, D. Alibhai, M. Mombrú and D. J. Fermín, *ACS Appl. Energy Mater.*, 2019, **2**, 3878–3885.
36 R. Nishikubo, H. Kanda, I. García-Benito, A. Molina-Ontoria, G. Pozzi, A. M. Asiri, M. K. Nazeeruddin and A. Saeki, *Chem. Mater.*, 2020, **32**, 6416–6424.
37 J. Li, X. Liu, J. Xu, J. Chen, C. Zhao, M. Salma Maneno, B. Zhang and J. Yao, *Sol. RRL*, 2019, **3**, 1900218.
38 R. Nie and S. I. Seok, *Small Methods*, 2020, **4**, 1900698.
39 R. Nie, H. Yun, M.-J. Paik, A. Mehta, B. Park, Y. C. Choi and S. I. Seok, *Adv. Energy Mater.*, 2018, **8**, 1701901.
40 R. Nie, B. Kim, S.-T. Hong and S. I. Seok, *ACS Energy Lett.*, 2018, **3**, 2376–2382.
41 Y. C. Choi, E. Hwang and D.-H. Kim, *APL Mater.*, 2018, **6**, 121108.
42 R. Nie, J. Im and S. I. Seok, *Adv. Mater.*, 2019, **31**, 1808344.
43 S. Toso, Q. A. Akkerman, B. Martín-García, M. Prato, J. Zito, I. Infante, Z. Dang, A. Moliterni, C. Giannini, E. Bladt, I. Lobato, J. Ramade, S. Bals, J. Buha, D. Spirito, E. Mugnaioli, M. Gemmi and L. Manna, *J. Am. Chem. Soc.*, 2020, **142**, 10198–10211.
44 U. V. Ghorpade, M. P. Suryawanshi, M. A. Green, T. Wu, X. Hao and K. M. Ryan, *Chem. Rev.*, 2023, **123**, 327–378.
45 E. J. Juarez-Perez, M. R. Leyden, S. Wang, L. K. Ono, Z. Hawash and Y. Qi, *Chem. Mater.*, 2016, **28**, 5702–5709.
46 Z. Li, Z. Zhu, C.-C. Chueh, J. Luo and A. K.-Y. Jen, *Adv. Energy Mater.*, 2016, **6**, 1601165.
47 X. Ji, T. Zhou, X. Ke, W. Wang, S. Wu, M. Zhang, D. Lu, X. Zhang and Y. Liu, *J. Mater. Chem. A*, 2020, **8**, 5163–5170.
48 R. Li, J. Zhang, M. Liu, S. K. Matta, J. Tian, Z. Deng, S. P. Russo, P. Vivo, Z. Zhou and H. Zhang, *Sol. RRL*, 2023, **7**, 2300031.
49 S. Collavini, A. Cabrera-Espinoza and J. L. Delgado, *Macromolecules*, 2021, **54**, 5451–5463.
50 A. Sadhu, M. Rai, T. Salim, X. Jin, J. M. R. Tan, S. W. Leow, M. G. Ahmed, S. Magdassi, S. G. Mhaisalkar and L. H. Wong, *Adv. Funct. Mater.*, 2021, **31**, 2103807.
51 H. Min, G. Kim, M. J. Paik, S. Lee, W. S. Yang, M. Jung and S. I. Seok, *Adv. Energy Mater.*, 2019, **9**, 1803476.
52 C. Hu, Y. Bai, S. Xiao, K. Tao, W. K. Ng, K. S. Wong, S. H. Cheung, S. K. So, Q. Chen and S. Yang, *Sol. RRL*, 2020, **4**, 2000270.
53 X. Yang, H. Xiang, J. Huang, C. Zhou, R. Ran, W. Wang, W. Zhou and Z. Shao, *J. Colloid Interface Sci.*, 2022, **628**, 476–485.
54 Z. Wang, M. A. Kamarudin, N. C. Huey, F. Yang, M. Pandey, G. Kapil, T. Ma and S. Hayase, *ChemSusChem*, 2018, **11**, 3941–3948.
55 X. Li, W. Zhang, X. Guo, C. Lu, J. Wei and J. Fang, *Science*, 2022, **375**, 434–437.
56 W. Hou, G. Han, T. Ou, Y. Xiao and Q. Chen, *Angew. Chem., Int. Ed.*, 2020, **59**, 21409–21413.
57 B. Wang, Q. Cheng, G. Huang, Y. Yue, W. Zhang, X. Li, Y. Li, W. Du, X. Liu, H. Zhang, Y. Zhang and H. Zhou, *Adv. Mater.*, 2023, **35**, 2207345.
58 B. P. Finkenauer, Y. Zhang, K. Ma, J. W. Turnley, J. Schulz, M. Gómez, A. H. Coffey, D. Sun, J. Sun, R. Agrawal, L. Huang and L. Dou, Amine-Thiol/Selenol Chemistry for Efficient and Stable Perovskite Solar Cells, *J. Phys. Chem. C*, 2023, **127**(2), 930–938.
59 Y. Zhang, Y. Han, Y. Xu, G. Yu, Y. Miao, C. Gao, X. Zhou, Y. Song and K.-J. Jiang, *Sustainable Energy Fuels*, 2021, **5**, 3700–3704.
60 C. Wang, Z. Zhu, G. Wang, X. Ding, Y. Chen, S. Xiao, X. Liu, X. Zhang and S. Wen, *ACS Sustainable Chem. Eng.*, 2022, **10**, 17318–17326.
61 J. Han, S. Luo, X. Yin, Y. Zhou, H. Nan, J. Li, X. Li, D. Oron, H. Shen and H. Lin, *Small*, 2018, **14**, 1801016.
62 E. A. Gaulding, X. Chen, Y. Yang, S. P. Harvey, B. To, Y.-H. Kim, M. C. Beard, P. C. Sercel and J. M. Luther, *ACS Mater. Lett.*, 2020, **2**, 1464–1472.
63 E. J. Lee, D.-H. Kim, R. P. H. Chang and D.-K. Hwang, *ACS Appl. Energy Mater.*, 2020, **3**, 10376–10383.
64 D. Li, T. Xia, W. Liu, G. Zheng, N. Tian, D. Yao, Y. Yang, H. Wang and F. Long, *Appl. Surf. Sci.*, 2022, **592**, 153206.
65 Q. Chen, J. Wu, J. T. Matondo, L. Bai, D. M. Maurice and M. Guli, *Sol. RRL*, 2020, **4**, 2000584.
66 N. Cheng, W. Li, M. Zhang, H. Wu, S. Sun, Z. Zhao, Z. Xiao, Z. Sun, W. Zi and L. Fang, *Curr. Appl. Phys.*, 2019, **19**, 25–30.
67 X. Wang, H. Huang, S. Du, P. Cui, Z. Lan, Y. Yang, L. Yan, J. Ji, B. Liu, S. Qu, Q. Zhang, X. Yue, X. Zhao and M. Li, *Sol. RRL*, 2022, **6**, 2200717.

68 S. Zhong, Z. Li, C. Zheng, X. Luo, J. Gao, X. Lu, X. Gao, L. Shui, S. Wu and J.-M. Liu, *Sol. RRL*, 2022, **6**, 2200088.
69 M.-S. Bae, Y. H. Chang, W. Lee, C.-S. Moon, S.-W. Kim, H.-S. Kim, J. Lim and T.-Y. Yang, *Energy Fuels*, 2023, **37**, 4608–4615.
70 Y. Yu, C. Wang, C. R. Grice, N. Shrestha, D. Zhao, W. Liao, L. Guan, R. A. Awni, W. Meng, A. J. Cimaroli, K. Zhu, R. J. Ellingson and Y. Yan, *ACS Energy Lett.*, 2017, **2**, 1177–1182.
71 Q. Jiang, D. Rebollar, J. Gong, E. L. Piacentino, C. Zheng and T. Xu, *Angew. Chem., Int. Ed.*, 2015, **54**, 7617–7620.
72 Q. Tai, P. You, H. Sang, Z. Liu, C. Hu, H. L. W. Chan and F. Yan, *Nat. Commun.*, 2016, **7**, 11105.
73 J. Liu, J. Shi, D. Li, F. Zhang, X. Li, Y. Xiao and S. Wang, *Synth. Met.*, 2016, **215**, 56–63.
74 G. Harbeke, *J. Phys. Chem. Solids*, 1963, **24**, 957–963.
75 A. Starczewska, M. Nowak, P. Szperlich, I. Bednarczyk, K. Mistewicz, M. Kepinska and P. Duka, *Frontiers in Optics 2014 (2014), paper JW3A.28*, Optica Publishing Group, 2014, p. JW3A.28.
76 T. Li, X. Wang, Y. Yan and D. B. Mitzi, *J. Phys. Chem. Lett.*, 2018, **9**, 3829–3833.
77 Y.-Y. Sun, J. Shi, J. Lian, W. Gao, M. L. Agiorgousis, P. Zhang and S. Zhang, *Nanoscale*, 2016, **8**, 6284–6289.
78 R. Nie, A. Mehta, B. Park, H.-W. Kwon, J. Im and S. I. Seok, *J. Am. Chem. Soc.*, 2018, **140**, 872–875.
79 Q. Sun, W.-J. Yin and S.-H. Wei, *J. Mater. Chem. C*, 2020, **8**, 12012–12035.
80 C. Li, X. Lu, W. Ding, L. Feng, Y. Gao and Z. Guo, *Acta Crystallogr., Sect. B: Struct. Sci.*, 2008, **64**, 702–707.
81 V. M. Goldschmidt, *Naturwissenschaften*, 1926, **14**, 477–485.
82 D. Tiwari, O. S. Hutter and G. Longo, *J. Phys.: Energy*, 2021, **3**, 034010.
83 P. Basera and S. Bhattacharya, *J. Phys. Chem. Lett.*, 2022, **13**, 6439–6446.
84 Z. Huo, S.-H. Wei and W.-J. Yin, *J. Phys. D: Appl. Phys.*, 2018, **51**, 474003.
85 A. Swarnkar, W. J. Mir, R. Chakraborty, M. Jagadeeswararao, T. Sheikh and A. Nag, *Chem. Mater.*, 2019, **31**, 565–575.
86 M.-G. Ju, J. Dai, L. Ma and X. C. Zeng, *Adv. Energy Mater.*, 2017, **7**, 1700216.
87 M. Ong, D. M. Guzman, Q. Campbell, I. Dabo and R. A. Jishi, *J. Appl. Phys.*, 2019, **125**, 235702.
88 S. Perera, H. Hui, C. Zhao, H. Xue, F. Sun, C. Deng, N. Gross, C. Milleville, X. Xu, D. F. Watson, B. Weinstein, Y.-Y. Sun, S. Zhang and H. Zeng, *Nano Energy*, 2016, **22**, 129–135.
89 M. L. Agiorgousis, Y.-Y. Sun, D.-H. Choe, D. West and S. Zhang, *Adv. Theory Simul.*, 2019, **2**, 1800173.
90 T. Gupta, D. Ghoshal, A. Yoshimura, S. Basu, P. K. Chow, A. S. Lakhnot, J. Pandey, J. M. Warrender, H. Efstathiadis, A. Soni, E. Osei-Agyemang, G. Balasubramanian, S. Zhang, S.-F. Shi, T.-M. Lu, V. Meunier and N. Koratkar, *Adv. Funct. Mater.*, 2020, **30**, 2001387.
91 X. Wei, H. Hui, C. Zhao, C. Deng, M. Han, Z. Yu, A. Sheng, P. Roy, A. Chen, J. Lin, D. F. Watson, Y.-Y. Sun, T. Thomay, S. Yang, Q. Jia, S. Zhang and H. Zeng, *Nano Energy*, 2020, **68**, 104317.
92 V. K. Ravi, S. H. Yu, P. K. Rajput, C. Nayak, D. Bhattacharyya, D. S. Chung and A. Nag, *Nanoscale*, 2021, **13**, 1616–1623.
93 S. P. Ramanandan, A. Giunto, E. Z. Stutz, B. Reynier, I. T. F. M. Lefevre, M. Rusu, S. Schorr, T. Unold, A. F. I. Morral, J. A. Márquez and M. Dimitrievska, *J. Phys.: Energy*, 2023, **5**, 014013.
94 J. W. Turnley, K. C. Vincent, A. A. Pradhan, I. Panicker, R. Swope, M. C. Uible, S. C. Bart and R. Agrawal, *J. Am. Chem. Soc.*, 2022, **144**, 18234–18239.
95 G. A. Wiegers, A. Meetsma, R. J. Haange and J. L. de Boer, *Acta Crystallogr.*, 1989, **C45**, 847–849.
96 T. Schmidt, K. Lischka and W. Zulehner, *Phys. Rev. B: Condens. Matter Mater. Phys.*, 1992, **45**, 8989.
97 L. Schmidt, *Phys. Lett. A*, 1970, **31**, 551–552.
98 S. Yamaoka, *J. Am. Ceram. Soc.*, 1972, **55**, 111.
99 S. Yamaoka and B. Okai, *Mater. Res. Bull.*, 1970, **5**, 789–794.
100 Y. Wang, N. Sato, K. Yamada and T. Fujino, *Shigen-to-Sozai*, 2000, **116**, 211–216.
101 N. Gross, Y.-Y. Sun, S. Perera, H. Hui, X. Wei, S. Zhang, H. Zeng and B. A. Weinstein, *Phys. Rev. Appl.*, 2017, **8**, 044014.
102 J. Yan, M. Greenblatt, A. Sahiner, D. Sills and M. Croft, *J. Alloys Compd.*, 1995, **229**, 216–222.
103 Y. Wang, N. Sato, K. Yamada and T. Fujino, *J. Alloys Compd.*, 2000, **311**, 214–223.
104 Y. Wang, N. Sato and T. Fujino, *J. Alloys Compd.*, 2001, **327**, 104–112.
105 K. V. Sopiha, C. Comparotto, J. A. Márquez and J. J. S. Scragg, *Adv. Opt. Mater.*, 2022, **10**, 2101704.
106 S. Niu, J. Milam-Guerrero, Y. Zhou, K. Ye, B. Zhao, B. C. Melot and J. Ravichandran, *J. Mater. Res.*, 2018, **33**, 4135–4143.
107 H. Zhang, X. Wu, K. Ding, L. Xie, K. Yang, C. Ming, S. Bai, H. Zeng, S. Zhang and Y.-Y. Sun, *Chem. Mater.*, 2023, **35**, 4128–4135.
108 R. Nie, K. S. Lee, M. Hu, M. J. Paik and S. I. Seok, *Matter*, 2020, **3**, 1701–1713.
109 A. Kaltzoglou, C. C. Stoumpos, A. G. Kontos, G. K. Manolis, K. Papadopoulos, K. G. Papadokostaki, V. Psycharis, C. C. Tang, Y.-K. Jung, A. Walsh, M. G. Kanatzidis and P. Falaras, *Inorg. Chem.*, 2017, **56**, 6302–6309.
110 C. Zhang, S. Teo, Z. Guo, L. Gao, Y. Kamata, Z. Xu and T. Ma, *Chem. Lett.*, 2019, **48**, 249–252.
111 V. I. Starosta, J. Kroutil and L. Beneš, *Cryst. Res. Technol.*, 1990, **25**, 1439–1442.
112 R. Nie, M. Hu, A. M. Risqi, Z. Li and S. I. Seok, *Adv. Sci.*, 2021, **8**, 2003172.
113 J. Xiong, Z. You, S. Lei, K. Zhao, Q. Bian, Y. Xiao and B. Cheng, *ACS Sustainable Chem. Eng.*, 2020, **8**, 13488–13496.
114 Y. C. Choi, D. U. Lee, J. H. Noh, E. K. Kim and S. I. Seok, *Adv. Funct. Mater.*, 2014, **24**, 3587–3592.

115 L. Zheng, D. Zhang, Y. Ma, Z. Lu, Z. Chen, S. Wang, L. Xiao and Q. Gong, *Dalton Trans.*, 2015, **44**, 10582–10593.
116 H. Kunioku, M. Higashi and R. Abe, *Sci. Rep.*, 2016, **6**, 32664.
117 S. Li, L. Xu, X. Kong, T. Kusunose, N. Tsurumachi and Q. Feng, *J. Mater. Chem. C*, 2020, **8**, 3821–3829.
118 S. M. Islam, C. D. Malliakas, D. Sarma, D. C. Maloney, C. C. Stoumpos, O. Y. Kontsevoi, A. J. Freeman and M. G. Kanatzidis, *Chem. Mater.*, 2016, **28**, 7332–7343.